ELSEVIER

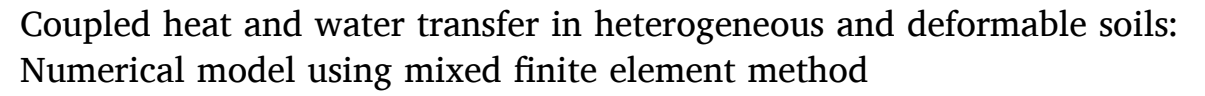
Contents lists available at ScienceDirect

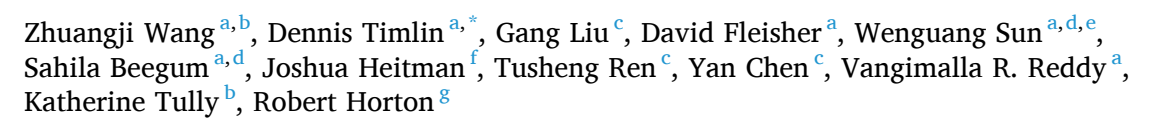
Journal of Hydrology

journal homepage: www.elsevier.com/locate/jhydrol



Research papers





- ^a Adaptive Cropping System Laboratory, USDA-ARS, Beltsville, MD 20705, USA
- b Department of Plant Science and Landscape Architecture, University of Maryland, College Park, MD 20742, USA
- ^c College of Land Science and Technology, China Agricultural University, Beijing 100193, China
- ^d Nebraska Water Center, University of Nebraska, Lincoln, NE 68588, USA
- ^e Natural Resource Ecology Laboratory, Colorado State University, Fort Collines, CO 80523, USA
- f Department of Crop and Soil Sciences, North Carolina State University, Raleigh, NC 27606, USA
- g Department of Agronomy, Iowa State University, Ames, IA 50011, USA

ARTICLE INFO

Keywords: Coupled heat and water transfer (CHWT) Mixed finite element method (FEM) Adaptive mesh refinement Soil deformation

ABSTRACT

We present a generic model framework for coupled heat and water transfer (CHWT) in deformable (non-rigid) soils with spatial variations of soil properties. The model backbone is a mixed finite element method (FEM), which solves the Philip and de Vries (1957) CHWT model and achieves conservation of mass and energy on both local and global scales. Spatial variations occur in soil hydraulic and thermal properties due to transient water content and temperature distributions. Based on the mixed FEM scheme, a gradient measure and a clustering model ("k-means") are proposed to trace the regions with large spatial variations of soil properties, and an adaptive mesh refinement technique is developed to improve the spatial resolution and simulation accuracy. Deformation perturbates local soil topography and alters transient soil water and temperature regimes in the deformed regions. A quasi-static deformation model is presented, and the deformation effects are incorporated into the mixed FEM scheme. When external load exists, soil deformation is simulated with an updated Lagrangian formulation, and the local water content and temperature variations due to soil volume changes are also updated in the CHWT model. Numerical examples, including thermally induced soil water transfer and water infiltration, illustrate the model ability to provide plausible CHWT results, especially the refined solutions near the wetting fronts and the water content and temperature distributions when the soil is deformable. In conclusion, the proposed model framework provides an effective pipeline to incorporate and process the spatial variations of soil properties and soil deformation in CHWT simulations.

1. Introduction

In coupled heat and water transfer (CHWT) simulations, despite the combination of multiple physical processes and nonlinearity, spatial variations of soil properties become a challenge in numerical modeling (Rienzner and Gandolfi, 2014; Shangguan et al., 2014). Following the development of large-scale geospatial models, an increasing amount of effort is invested to address physical processes in porous media with spatial heterogeneities (Hou and Wu, 1997; Hou et al., 1999).

Spatial variations of soil properties include two components. (a) Soil

heterogeneity is due to the non-uniformity of soil texture and structure, such as saturated hydraulic conductivity, which is usually expressed using random field methods, such as Karhunen–Loeve expansion (Li et al., 2019; Phoon et al., 2002; Phoon et al., 2005) and Markov chain Monte Carlo (MCMC, Winkler, 2003). (b) Transient variation of soil properties is caused by instantaneous fluctuations in soil water content or temperature values, which occurs in actual (unsaturated) hydraulic conductivity or apparent thermal properties even if the soil texture and structure are uniform (Lu et al., 2014; Xie et al., 2018). Although existing studies focus on soil heterogeneity (He and Ren, 2005; He and

E-mail address: dennis.timlin@usda.gov (D. Timlin).

 $^{^{\}ast}$ Corresponding author.

Ren, 2009; Li et al., 2016; Luo et al., 2022), the magnitude of transient variations can be much larger. For example, spatial variations of saturated hydraulic conductivity may have an order of 10⁴-10⁵ (He and Ren, 2006), while transient variations of unsaturated hydraulic conductivity can have a magnitude $> 10^{10}$, due to the nonlinear relations between soil water content and hydraulic conductivity [see the exponential K(h, x)] T) function in Table 1]. Moreover, locations with large transient variations of soil properties may change during soil heat and water redistribution. Thus, transient variation of soil properties becomes a temporalspatial factor in vadose zone soil models that should be emphasized under diurnal and seasonal weather conditions. In contrast, heterogeneity is mainly considered in saturated zones or in reservoir models, where all pores are filled by water or petroleum. Nonlinearities of hydraulic conductivity in reservoir models are mainly expressed via the mobility of water or petroleum, as well as the oil-cut or water-cut in liquid fluxes (Efendiev and Hou, 2009), which has a narrow fluctuation range compared to the nonlinearities in vadose zone soils.

Spatial variations of soil properties are related to soil deformation. When a uniform soil is deformed, soil structure, porosity and bulk density near the deformed regions are changed, leading to heterogeneities in soil hydraulic and thermal properties. Moreover, local volumetric water content is changed due to soil compaction or expansion, which leads to transient variations in soil hydraulic properties. Such transient variations can be mitigated under soil water and heat redistributions between the deformed region and its neighboring area, while the deformation induced heterogeneity will persist. The effects of deformation induced heterogeneity on soil properties can be represented by systematic constitutive relations. However, most of the existing studies report experimental and empirical results. For example, McCullough et al. (2001) performed a field study of hydraulic conductivity under a range of soil bulk density. Tian et al. (2021) proposed empirical equations of soil water characteristic curves with changing soil bulk density. Zhang et al. (2023) reported the use of thermo-time domain reflectometry in measuring soil hydraulic and thermal properties during soil shrinking and swelling.

Adaptively incorporating both soil heterogeneity and transient variations of soil properties into CHWT models, and providing high resolution simulations are not fully studied yet. Existing numerical methods mainly address soil heterogeneity, such as the homogenization theory or multiscale models (He and Ren, 2005; He and Ren, 2009; Li et al., 2016; Luo et al., 2022). Furthermore, implementing soil deformation with CHWT remains a challenge in soil physics and vadose zone hydrology (Tian et al., 2019), where quantifying spatial variations of soil properties is the prerequisite. Including spatial variations of soil properties and soil deformation requires sophisticated designs for the numerical solvers and the overall model architecture, which are not fully supported by existing 2D soil and crop simulators, such as HYDRUS or 2DSOIL (Simunek et al., 2016; Timlin et al., 1996).

Thus, the objective of this study is to develop a numerical model framework that can incorporate spatial variations of soil properties and soil deformation into CHWT models and demonstrate the model performance with numerical and application examples. The starting point is a baseline numerical solver for CHWT, which performs computation in irregular and moving mesh grids, and conserves mass and energy at both local and global scales. Mixed finite element methods (mixed FEM) satisfy the two requirements and have been applied to soil water transfer (Chounet et al., 1998; Putti and Sartoretto, 2009). However, implementation of mixed FEM in CHWT problems has not been fully studied in soil physics.

Therefore, the main objective is divided into three steps. (Step A) Formulate mixed FEM as the baseline numerical solver for CHWT in Section 2. (Step B) Design a mesh refinement technique to trace the spatial variations of soil properties and improve the accuracy and resolution of CHWT simulations in Section 3. (Step C) Incorporate soil deformation in the CHWT model via a soil mechanics module and a

mesh deformation technique in Section 4. Step (A) establishes the foundation, and the objective of this study is fulfilled in Steps (B) and (C) based on Step (A). Soil deformation in Step (C) also depends on the mesh refinement technique in Step (B), for deformation can induce soil property changes.

Illustrative examples are provided along with the model development. Sections 2-4 presents three relatively independent examples, and each example is designed to emphasize the accomplishment of that section. When the model development is complete, an application example is provided in Section 5. All the examples presented are typical vadose zone problems or abstracted from real world applications to ensure their representativeness, but the proposed model framework is not limited to specific problems or applications. A computer implementation is developed using the MATLAB programming language (Mathworks, MA). Detailed numerical techniques and model validations against benchmark simulations and experiments are provided in the supplementary material. Because theories and constitutive relations for soil hydraulic and thermal properties under elastic-plastic deformation have not been fully established, assumptions are made and clarified as the model is presented. However, newly discovered constitutive relations can be easily embedded as add-on functions without substantial changes of the model architecture.

2. The mixed finite element scheme for coupled heat and water transfer (Step A)

Despite the mathematical theory of mixed FEM (Brezzi, 1974), the mixed FEM numerical scheme for CHWT has not been formulated. In this section, we establish the mixed FEM scheme as the baseline model. Different from existing methods (Chounet et al., 1999), liquid water, vapor, conductive heat fluxes, and soil water content and temperature, are discretized and solved from a single system of equations. Therefore, soil heat transfer and soil water transfer are "fully coupled".

2.1. Coupled heat and water transfer and the mixed finite element scheme

Philip and de Vries (1957) model is a widely used formulation in CHWT problems (Sophocleous, 1979; Milly, 1982; Nassar and Horton, 1989; Nassar and Horton, 1997). The governing equations are given in Eq. (1), from which the soil water potential (h, cm) and soil temperature (T, K) are solved as functions of time (t, s) and space [(x, y), cm]. Local thermal and water potential equilibrium at the liquid water-vapor interface is assumed (Vanderborght et al., 2017).

$$q_{\nu} + D_{m\nu}(h, T)\nabla h + D_{T\nu}(h, T)\nabla T = 0$$
 (1b)

$$q_h + \lambda(h, T)\nabla T = 0 \tag{1c}$$

$$q_{h} + \lambda(h, T)\nabla T = 0 \qquad (1c)$$

$$-\nabla \cdot q_{l} - \nabla \cdot q_{v} = C_{\theta\theta}(h, T)\partial_{t}h + C_{\theta T}(h, T)\partial_{t}T \qquad (1d)$$

$$-\nabla \cdot q_{h} - c_{l}\rho_{l}(T - T_{0})\nabla \cdot q_{l} = C_{T\theta}(h, T)\partial_{t}h + C_{TT}(h, T)\partial_{t}T \qquad (1e)$$

$$-\nabla \cdot q_h - c_l \rho_l (T - T_0) \nabla \cdot q_l$$

$$-[L_0 + c_v (T - T_0)] \rho_l \nabla \cdot q_v$$

$$= C_{T\theta}(h, T) \partial_r h + C_{TT}(h, T) \partial_t T \quad (1e)$$

Eq. (1a) is a generalized Darcy-Buckingham Law, where $q_l(\text{cm s}^{-1})$ is the liquid water flux density, K(h, T) (cm s⁻¹) is the soil hydraulic conductivity, $D_{Tl}(\text{cm}^2 \text{ s}^{-1} \text{ K}^{-1})$ is the liquid water diffusion coefficient under temperature gradients, $\nabla = \left[\partial_x, \partial_y\right]^T$ is the differential operator. $-K(h,T)\hat{\mathbf{y}}$ represents the gravitational liquid water flux. Hereafter, if a 2D soil spatial domain is in a vertical plane, the y-axis represents the vertical coordinate and \hat{y} is the unit vertical vector. If a 2D soil spatial domain is in a horizontal plane, the gravity term " $-K(h, T)\hat{y}$ " is ignored and both x-axis and y-axis are perpendicular to the local gravity. Eq. (1b) is analogous to Fick's Law, where $q_{\nu}({\rm cm\,s^{-1}})$ is the vapor flux density, and $D_{mv}(h,T)$ (cm s⁻¹) and $D_{Tv}(h,T)$ (cm² s⁻¹ K⁻¹) are coefficients of vapor flux under water potential and temperature gradients. A vapor diffusion enhancement included in $D_{T\nu}(h,T)$ quantifies the vapor transfer assisted by liquid water islands within the soil profile (Cass et al., 1984). Eq. (1c) represents Fourier's Law, where $q_h(\mathrm{W\,cm^{-2}})$ is the conductive heat flux density and $\lambda(\mathrm{W\,cm^{-1}\,K^{-1}})$ is the soil thermal conductivity.

Eqs. (1d) and (1e) present the conservation of mass and energy in the soil profile, where $C_{\theta\theta}(\mathrm{cm^{-1}})$, $C_{\theta T}(\mathrm{K^{-1}})$, $C_{T\theta}(\mathrm{J\,cm^{-3}\,cm^{-1}})$ and $C_{TT}(\mathrm{J\,cm^{-3}\,K^{-1}})$ are the capacity coefficients for h and T, changing with respect to soil water content $(\theta,\,\mathrm{cm^3\,cm^{-3}})$ and soil temperature (see the supplement material). ∂_t is the partial differentiation with respect to time t(s). $c_l \approx 4.187\mathrm{J\,g^{-1}\,K^{-1}}$ is the specific heat of liquid water. $c_v \approx 1.864(\mathrm{J\,g^{-1}\,K^{-1}})$ is the specific heat of water vapor. $L_0 \approx 2453(\mathrm{J\,g^{-1}\,at\,20^{\circ}\,C})$ is the heat of vaporization of water at a reference temperature T_0 (in this study, $T_0 = 20^{\circ}\,\mathrm{C}$). $\rho_l \approx 1.0\mathrm{g\,cm^{-3}}$ is the density of liquid water. Solutions of Eq. (1) can be presented based on either soil water potential or soil water content converted using a soil water characteristic curve. A detailed derivation of Eq. (1) is given in the supplementary material, which is a summary of Nassar and Horton (1997), Heitman et al. (2008), Wang et al. (2017) and Wang et al. (2022).

The CHWT model is a mixed formulation, where Eqs.1a-c are vector equations representing fluxes and Eqs. (1d and 1e) are scalar equations representing the conservation laws (Boffi et al., 2013). To obtain the mixed FEM scheme, let Ω be a given soil profile and let $H(\operatorname{div},\Omega)=\left\{\phi\in H(\Omega): \int_\Omega \phi^2 ds < \infty, \int_\Omega (\nabla \cdot \phi)^2 ds < \infty\right\}$ be the Hilbert space on Ω , where the vector (flux) functions ϕ and their divergence $\nabla \cdot \phi$ are square-integrable. Then, the trial spaces for the vector equations and scalar equations are $V=\{\phi\in H(\operatorname{div},\Omega): \widehat{n}\cdot\phi=g \text{ on }\partial\Omega\}$ and $W=\mathscr{L}^2(\Omega)=\{\psi:\int_\Omega \psi^2 ds < \infty\}$, respectively, where g is the flux boundary conditions, \widehat{n} is the outer normal vector of $\partial\Omega$, and $\mathscr{L}^2(\Omega)$ is the space of (scalar) Lebesgue square-integrable functions. Let $V_0=\{v\in H(\operatorname{div},\Omega):v\cdot\widehat{n}=0 \text{ on }\partial\Omega\}$ be the test space for the vector equations. Then, the CHWT problem in Eq. (1) can be transformed into a saddle-point problem, where the goal is to find $(q_l,q_v,q_h,h,T)\in V^3 \bigotimes W^2$ satisfying Eq. (2).

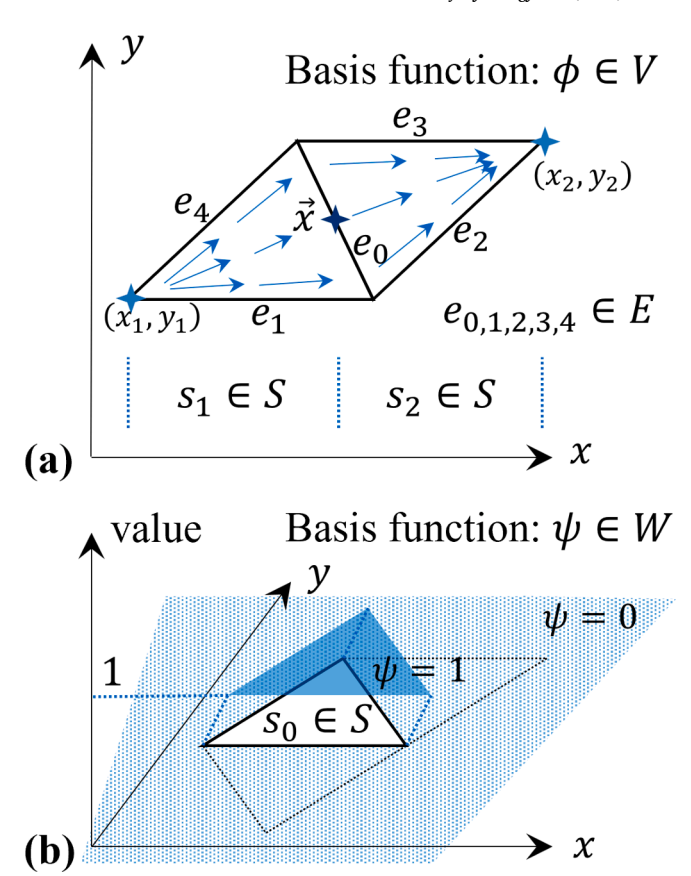


Fig. 1. Basis functions in the mixed FEM scheme. (a) shows a zero order Raviart–Thomas (RT_0) function $\phi \in V$ representing a "unit flux density" on the normal direction of edge $e_0 \in E$, from surface $s_1 \in S$ to surface $s_2 \in S$. \overrightarrow{x} is the middle point of e_0 . (b) shows a piecewise constant basis function $\psi \in W$ representing the scalar quantities, such as soil water potential, soil water content or soil temperature, within each surface. The example piecewise constant basis function in (b) takes value $\psi = 1$ on the solid element $s_0 \in S$, while $\psi = 0$ otherwise.

$$\begin{cases}
\langle q_{l}, \phi \rangle - \langle \nabla \cdot \phi, K(h, T)h \rangle - \langle \nabla \cdot \phi, D_{Tl}(h, T)T \rangle &= -\langle K(h, T)\widehat{y}, \phi \rangle, & \forall \phi \in V_{0} \\
\langle q_{v}, \phi \rangle - \langle \nabla \cdot \phi, D_{mv}(h, T)h \rangle - \langle \nabla \cdot \phi, D_{Tv}(h, T)T \rangle &= 0, & \forall \phi \in V_{0} \\
\langle q_{h}, \phi \rangle - \langle \nabla \cdot \phi, \lambda(h, T)T \rangle &= 0, & \forall \phi \in V_{0} \\
-\langle \nabla \cdot q_{l}, \psi \rangle - \langle \nabla \cdot q_{v}, \psi \rangle &= \langle C_{\theta\theta}(h, T)\partial_{t}h, \psi \rangle + \langle C_{\theta T}(h, T)\partial_{t}T, \psi \rangle, & \forall \psi \in W \\
-\langle \nabla \cdot q_{h}, \psi \rangle - \langle c_{l}\rho_{l}(T - T_{0})\nabla \cdot q_{l}, \psi \rangle &= \langle C_{T\theta}(h, T)\partial_{t}h, \psi \rangle + \langle C_{TT}(h, T)\partial_{t}T, \psi \rangle, & \forall \psi \in W
\end{cases}$$

$$(2)$$

 $V^3 \bigotimes W^2$ is a 5D trial functional space for the mixed FEM scheme proposed in this study, and $\langle \cdot, \cdot \rangle$ represents the inner product for vectors, $\langle a, b \rangle = \int_{\Omega} (a^T b) ds$, or scalars, $\langle a, b \rangle = \int_{\Omega} (ab) ds$.

For numerical implementation, the soil profile Ω can be discretized into a triangular mesh grid. In the mesh grid, three sets (E, N, S) represent the edges, nodes, and surfaces (the element in traditional FEM), and the total numbers of edges, nodes and surfaces are n_E , n_N , and n_S . Given the triangular grid, the trial and test spaces should be restricted to certain types of functions to ensure the solvability of the saddle-point problem in Eq. (2) and the well-posedness of the numerical system. A commonly used basis function for V is the zero order Raviart-

Thomas (RT_0) function on each edge, and the basis function for W is the piecewise constant function on each surface.

A graphical definition of the RT₀ function and the piecewise constant basis function in a triangular grid is given in Fig. 1. In Fig. 1a, the RT₀ basis function for edge $e_0 \in E$ is shown as follows.

$$\phi_{e0}(x,y) = \begin{cases} [x - x_1 \quad y - y_1]^T / 2A_{s1} \quad (x,y) \in s_1 \\ [x_2 - x \quad y_2 - y]^T / 2A_{s2} \quad (x,y) \in s_2 , \phi_{e0} \in V \\ 0 \quad \text{otherwise} \end{cases}$$
 (3)

 A_{s1} and A_{s2} are the areas of surfaces s_1 and s_2 . At the middle point of e_0 (dark blue \spadesuit), $\phi_{e0}(\overrightarrow{x}) \cdot \widehat{n}_{e0} l_{e0} = 1$, where \widehat{n}_{e0} is the normal vectors of e_0

and l_{e0} is the length e_0 . However, the vector field of ϕ_{e0} is parallel to all other edges e_k , $\forall k=1,2,3,4$. Thus, ϕ_{e0} represents a "unit flux density" across edge e_0 . For the liquid water flux, vapor flux and conductive heat flux in Eq. (1), their components on edge e_0 can be expressed by ϕ_{e0} with some coefficients. Extending the definition of the RT₀ basis function to all the edges, liquid water flux, vapor flux and conductive heat flux on the entire soil profile can be expressed in Eq. (4), where $\hat{q}^t_{l,e}$, $\hat{q}^t_{v,e}$, and $\hat{q}^t_{h,e}$ are the liquid water, vapor and conductive heat flux values on edge e at time t.

$$\begin{cases} q_{l}(x, y, t) = \sum_{e \in E} \widehat{q}_{l,e}^{t} \phi_{e}(x, y) \\ q_{v}(x, y, t) = \sum_{e \in E} \widehat{q}_{v,e}^{t} \phi_{e}(x, y), \phi_{e} \in V \\ q_{h}(x, y, t) = \sum_{e \in E} \widehat{q}_{h,e}^{t} \phi_{e}(x, y) \end{cases}$$
(4)

Similarly, in Fig. 1b, the piecewise constant function for surface $s_0 \in S$ has the scalar form in Eq. (5). Each basis function $\psi_s \in W$ achieves the value "1" only on one surface of the triangular grid.

$$\psi_{s0}(x,y) = \begin{cases} 1 & (x,y) \in s_0 \\ 0 & \text{otherwise} \end{cases}, \psi_{s0} \in W$$
 (5)

Extending the definition of the piecewise constant basis functions to all the surfaces, the FEM expansions of soil water potential and soil temperature can be given in Eq. (6), where \hat{h}_s^t and \hat{T}_s^t are the soil water potential and temperature values of surface s at time t.

$$\begin{cases} h(x, y, t) = \sum_{s \in S} \widehat{h}_s^t \psi_s(x, y) \\ T(x, y, t) = \sum_{s \in S} \widehat{T}_s^t \psi_s(x, y) \end{cases}, \psi_s \in W$$
(6)

Insert Eqs. (4) and (6) into the saddle-point problem in Eq. (2), the spatial discretization of the CHWT model is obtained. Temporal differentiation can be approximated using the implicit Euler scheme, and local linearization for each time step can be performed using Picard iteration (see the supplementary material). Then, the fully discretized CHWT model is presented in Eq. (7). For conciseness, the summation convention on subscripts $e \in E$ and $s \in S$ is assumed, and independent variables for the coefficient functions, such as K, D_{Tl} , etc., are omitted.

different values.

In principle, the inner products in Eq. (7) correspond to integrations over the entire soil profile Ω , i.e., $\langle \phi_e, \phi_{e'} \rangle = \int_{\Omega} \phi_e^T \phi_e ds$, $\langle \nabla \cdot \phi_{e'}, \psi_s \rangle = \int_{\Omega} (\nabla \cdot \phi_{e'}) \psi_s ds$, $\langle \psi_s, \psi_s' \rangle = \int_{\Omega} \psi_s \psi_s ds$, and $\langle \hat{y}, \phi_{e'} \rangle = \int_{\Omega} \hat{y}^T \phi_{e'} ds$. However, using the basis functions in Eqs. (3) and (5), those integrands achieve non-zero values only on one or two surfaces, and hence the integrals can be computed as polynomials of the vertex coordinates of those surfaces. Moreover, the fully discretized CHWT model in Eq. (7) is a linear system with a sparse coefficient matrix. Therefore, solving Eq. (7) is not computationally expensive. After solving the unknowns $\left(\hat{q}_{l,e}^{t+1}, \hat{q}_{v,e}^{t+1}, \hat{$

2.2. Illustrative example

A thermally induced water redistribution is presented to demonstrate the workability of the mixed FEM scheme. "Thermally induced" means the soil temperature gradient serves as the driving force for vapor transfer. The combination of liquid water evaporation, vapor transfer and vapor condensation in the soil sample becomes a path for soil water redistribution. Thus, the coupling of heat transfer and water transfer is emphasized in both physical and numerical perspective.

For the numerical settings, consider a horizontally placed 2D rectangular soil sample, which is 30 cm in width (*x*-axis) and 60 cm in length (*y*-axis). Hereafter, the directions of *x*-axis and *y*-axis are denoted in the associated figures. The soil physical properties are listed in Table 1. Values of the soil physical properties were supported by experiments, and soil heat and water transfer with those values were validated with both experimental and numerical studies (see the supplementary material for validation examples, also see Heitman et al., 2007; Heitman et al., 2008; Wang et al., 2017; Wang et al., 2022).

Suppose the soil sample has a uniform initial water content $\theta_{ini} = 0.15 \text{ cm}^3 \text{ cm}^{-3}$ and temperature $T_{ini} = 25.0^{\circ} \text{ C}$. No heat flux occurs on the two boundaries along the long side of the soil sample (x=0,x=30). At one boundary along the short side of the soil sample (y=0), the boundary temperature linearly decreases from 25° C to 10° C , $T_{y=0} = 25-0.5x$. On the opposite side (y=60), the boundary temperature linearly decreases from 40° C to 25° C , $T_{y=60} = 40-0.5x$. All the

$$\begin{cases} \langle \phi_{e}, \phi_{e'} \rangle \widehat{q}_{l,e}^{t+1} - K \langle \nabla \cdot \phi_{e'}, \psi_{s} \rangle \widehat{h}_{s}^{t+1} - D_{Tl} \langle \nabla \cdot \phi_{e'}, \psi_{s} \rangle \widehat{T}_{s}^{t+1} & = -K \langle \widehat{y}, \phi_{e'} \rangle, \qquad \forall \phi_{e'} \in V_{0} \\ \langle \phi_{e}, \phi_{e'} \rangle \widehat{q}_{v,e}^{t+1} - D_{mv} \langle \nabla \cdot \phi_{e'}, \psi_{s} \rangle \widehat{h}_{s}^{t+1} - D_{Tv} \langle \nabla \cdot \phi_{e'}, \psi_{s} \rangle \widehat{T}_{s}^{t+1} & = 0, \qquad \forall \phi_{e'} \in V_{0} \\ \langle \phi_{e}, \phi_{e'} \rangle \widehat{q}_{h,e}^{t+1} - \lambda \langle \nabla \cdot \phi_{e'}, \psi_{s'} \rangle \widehat{T}_{s}^{t+1} & = 0, \qquad \forall \phi_{e'} \in V_{0} \\ \langle \nabla \cdot \phi_{e}, \psi_{s'} \rangle \Delta t \widehat{q}_{l,e}^{t+1} + \langle \nabla \cdot \phi_{e}, \psi_{s'} \rangle \Delta t \widehat{q}_{v,e}^{t+1} & = C_{\theta \theta} \widehat{h}_{s}^{t} \langle \psi_{s}, \psi_{s'} \rangle + C_{\theta T} \widehat{T}_{s}^{t+1} \langle \psi_{s}, \psi_{s} \rangle + C_{\theta T} \widehat{T}_{s}^{t+1} \langle \psi_{s}, \psi_{s} \rangle \Delta t \widehat{q}_{v,e}^{t+1} & = C_{\theta \theta} \widehat{h}_{s}^{t} \langle \psi_{s}, \psi_{s'} \rangle \Delta t \widehat{q}_{l,e}^{t+1} + [L_{0} + c_{v}(T - T_{0})] \rho_{l} \langle \nabla \cdot \phi_{e}, \psi_{s'} \rangle \Delta t \widehat{q}_{v,e}^{t+1} & = C_{TT} \widehat{T}_{s}^{t} \langle \psi_{s}, \psi_{s'} \rangle \\ + \langle \nabla \cdot \phi_{e}, \psi_{s'} \rangle \Delta t \widehat{q}_{h,e}^{t+1} + C_{T\theta} \widehat{h}_{s}^{t+1} \langle \psi_{s}, \psi_{s'} \rangle + C_{TT} \widehat{T}_{s}^{t+1} \langle \psi_{s}, \psi_{s'} \rangle & = C_{T\theta} \widehat{h}_{s}^{t} \langle \psi_{s}, \psi_{s'} \rangle \\ + C_{TT} \widehat{T}_{s}^{t} \langle \psi_{s}, \psi_{s'} \rangle & = C_{T\theta} \widehat{h}_{s}^{t} \langle \psi_{s}, \psi_{s'} \rangle \\ + C_{TT} \widehat{T}_{s}^{t} \langle \psi_{s}, \psi_{s'} \rangle & = C_{T\theta} \widehat{h}_{s}^{t} \langle \psi_{s}, \psi_{s'} \rangle \\ + C_{TT} \widehat{T}_{s}^{t} \langle \psi_{s}, \psi_{s'} \rangle & = C_{T\theta} \widehat{h}_{s}^{t} \langle \psi_{s}, \psi_{s'} \rangle \\ + C_{TT} \widehat{T}_{s}^{t} \langle \psi_{s}, \psi_{s'} \rangle & = C_{T\theta} \widehat{h}_{s}^{t} \langle \psi_{s}, \psi_{s'} \rangle \\ + C_{TT} \widehat{T}_{s}^{t} \langle \psi_{s}, \psi_{s'} \rangle & = C_{T\theta} \widehat{h}_{s}^{t} \langle \psi_{s}, \psi_{s'} \rangle \\ + C_{TT} \widehat{T}_{s}^{t} \langle \psi_{s}, \psi_{s'} \rangle & = C_{T\theta} \widehat{h}_{s}^{t} \langle \psi_{s}, \psi_{s'} \rangle \\ + C_{TT} \widehat{T}_{s}^{t} \langle \psi_{s}, \psi_{s'} \rangle & = C_{T\theta} \widehat{h}_{s}^{t} \langle \psi_{s}, \psi_{s'} \rangle \\ + C_{TT} \widehat{T}_{s}^{t} \langle \psi_{s}, \psi_{s'} \rangle & = C_{T\theta} \widehat{h}_{s}^{t} \langle \psi_{s}, \psi_{s'} \rangle \\ + C_{TT} \widehat{T}_{s}^{t} \langle \psi_{s}, \psi_{s'} \rangle & = C_{T\theta} \widehat{h}_{s}^{t} \langle \psi_{s}, \psi_{s'} \rangle \\ + C_{TT} \widehat{T}_{s}^{t} \langle \psi_{s}, \psi_{s'} \rangle & = C_{T\theta} \widehat{h}_{s}^{t} \langle \psi_{s}, \psi_{s'} \rangle \\ + C_{TT} \widehat{T}_{s}^{t} \langle \psi_{s}, \psi_{s'} \rangle & = C_{T\theta} \widehat{h}_{s}^{t} \langle \psi_{s}, \psi_{s'} \rangle \\ + C_{TT} \widehat{T}_{s}^{t} \langle \psi_{s}, \psi_{s'} \rangle & = C_{T\theta} \widehat{h}_{s}^{t} \langle \psi_{s}, \psi_{s'} \rangle \\ + C_{TT} \widehat{$$

In Eq. (7), the superscript t indicates the current time step, and t+1 indicates the next time step. Δt is the time step. On the left-hand side of the last equation, the differences between the current temperature and the reference temperature $(T-T_0)$ should be evaluated using the temperature values in the up-stream directions to satisfy the "upwind scheme". Because the up-stream directions of liquid water flux q_l and vapor flux q_v may not be the same, the two $(T-T_0)$ terms may take

boundaries are impermeable to liquid water and vapor fluxes. The simulation is performed until the steady state is reached, and the final soil temperature and water content regimes, as well as the heat and water fluxes are presented in Fig. 2.

The spatial distributions of soil water content and soil temperature are presented in Fig. 2a and b. Low temperature regions tend to have high water contents. That is because liquid water in soil vaporizes near high temperature regions, transports to low temperature regions

Table 1
Physical Properties of the Ida Silt (Heitman et al., 2008).

Ida Silt (fine-silty, mixed, superactive, calcareous, mesic Typic Udorthents)							
Soil Textural Properties							
Sand $(f_{sand}, g g^{-1})$	0.022						
Silt (f_{silt}, gg^{-1})	0.729						
Clay $\left(f_{clay}, \mathrm{g} \mathrm{g}^{-1}\right)$	0.249						
Organic matter $(g g^{-1})$	0.044						
Bulk density $(\rho_b, g \text{ cm}^{-3})$	1.20						
Hydraulic Properties							
Saturated water content $(\theta_s, \text{ cm}^3 \text{ cm}^{-3})$	0.547						
Saturated hydraulic conductivity at $T_0(K_s, \text{cm s}^{-1})$	3.80×10^{-4}						
Water characteristic function	$h = -13.0 \times (\theta/\theta_s)^{-6.53}$						
Hydraulic conductivity $(K, \text{ cm s}^{-1})$	$K = \left[\mu(T_0)/\mu(T)\right] \times (\theta/\theta_s)^{16.06} K_s \dagger$						
Thermal Properties							
Thermal conductivity $(\lambda, W cm^{-1} K^{-1})$	$\lambda = 0.00952 + 0.0431\theta + 0.06\sqrt{\theta}$						

 $\dagger \mu(T)$ represents the dynamic viscosity of water, as a function of soil temperature.

following the temperature gradient and condenses. Hence, "thermally induced soil water transfer" is demonstrated. Using the mixed FEM scheme, the water content and temperature are computed on each surface, rather than for each node or edge. Therefore, the soil temperature values near the boundaries may not exactly match the temperature given at the boundaries. For example, the minimum and the maximum temperature values in the soil sample are 12.3°C and 37.8°C, while the

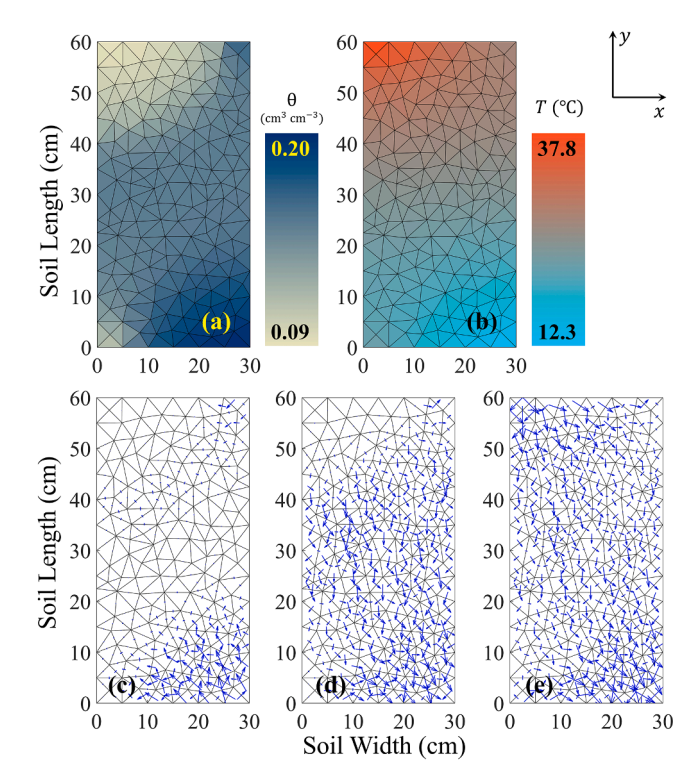


Fig. 2. Simulation results of the CHWT model using the new mixed FEM scheme. Five quantities are directly solved from the mixed FEM scheme. They are (a) soil water content (or soil water potential), (b) soil temperature, (c) liquid water flux, (d) vapor flux, and (e) conductive heat flux. For optimal presentation, the length of the vectors in subfigures (c), (d) and (e) are scaled individually, such that comparisons of vector length are not valid.

pre-specified minimum and the maximum boundary temperature values are 10.0° C and 40.0° C (at two corners of the computing domain).

Liquid water flux, vapor flux and conductive heat flux are presented in Fig. 2c-e, and the flux density values range $0-9.16 \times 10^{-7} \text{ cm s}^{-1}$, $0\text{-}9.35\times~10^{-7}~\text{cm}\,\text{s}^{-1}\text{,}\,$ and $\,0\text{-}0.25\,\text{W}\,\text{cm}^{-2}\text{,}\,$ respectively. The flux directions and flux density values are plotted as vectors across each interior edge. Two regions with relatively large liquid water fluxes exist in Fig. 2c. The first region is near the low temperature corner with high soil water content (x = 30, y = 0). The second region forms an arc from (x = 0) 0, y = 40) to (x = 30, y = 60), where the water potential gradient is relatively large, but the soil water content, hence the hydraulic conductivity, is relatively low. In Fig. 2d, the vapor flux magnitude near the high temperature corner (x = 0, y = 60) achieves the smallest value due to the lack of soil water, despite the large soil temperature gradients in that region. For the conductive heat flux in Fig. 2e, the maximum flux magnitudes are achieved near the two corners with the maximum and minimum temperature values (x = 0, y = 60) and (x = 30, y = 0), and hence, the conductive heat flux magnitude is roughly proportional to the soil temperature gradients.

This example illustrates the ability of using mixed FEM scheme to solve soil CHWT problems. Comparisons of the mixed FEM scheme on some (simpler) benchmark numerical or experimental studies can be found in the supplementary material.

2.3. Additional remarks for the mixed finite element scheme

In the mixed FEM scheme, flux values are computed on each edge, while soil water potential, water content and temperature are computed on each surface. Thus, the conservation of mass and energy are satisfied locally in each surface as well as globally in the whole soil profile. In contrast, traditional FEM only supports global conservation (see the numerical fluctuations in Fig. 1, Pan et al., 1996). Finite difference method (FDM) supports global and local conservation, but it is usually applied in rectangular mesh grids. Convective and latent heat fluxes are not explicitly presented in Fig. 2, because they are "secondary quantities" relying on liquid water and vapor transfer. In other words, convective and latent heat fluxes are determined after the liquid water and vapor fluxes are solved.

To enhance the simulation performance, a modification is applied to the mixed FEM scheme. Consider the discretized liquid water flux across edge e_0 in Fig. 1a.

$$\sum\nolimits_{k=0}^{4} \langle \phi_{ek}, \phi_{e0} \rangle \widehat{q}_{l,ek}^{t+1} - \left(K_{s1} \widehat{h}_{s1}^{t+1} - K_{s2} \widehat{h}_{s2}^{t+1} \right) - \left(D_{Tl,s1} \widehat{T}_{s1}^{t+1} - D_{Tl,s2} \widehat{T}_{s2}^{t+1} \right) = 0 \tag{8}$$

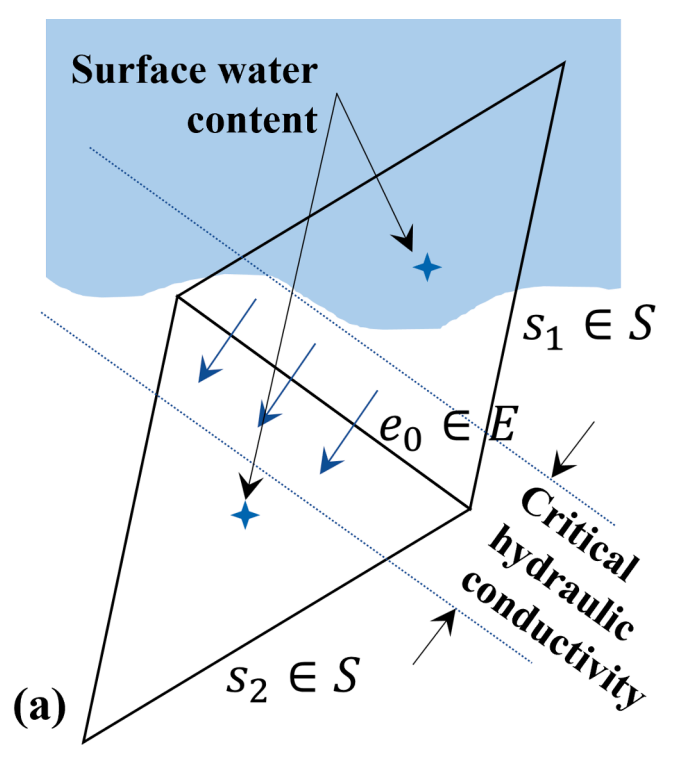
When the soil water potential difference between the two adjoined surfaces is large, or when the hydraulic conductivity function is not appropriately chosen, there is a possibility that $|\hat{h}_{s1}^{t+1}/\hat{h}_{s2}^{t+1}| < |K_{s1}/K_{s2}|$, even if $\hat{h}_{s1}^{t+1} > \hat{h}_{s2}^{t+1}$, which implies $K_{s1}\hat{h}_{s1}^{t+1} < K_{s2}\hat{h}_{s2}^{t+1}$, and hence the direction of liquid water transfer is wrongly determined. To avoid that, the effective conductivity (K_{eff}) and diffusivity (D_{Tleff}) are adopted.

$$\sum\nolimits_{k=0}^{4} \langle \phi_{ek}, \phi_{e0} \rangle \widehat{q}_{l,ek}^{t+1} - K_{\rm eff} (\widehat{h}_{s1}^{t+1} - \widehat{h}_{s2}^{t+1}) - D_{Tl,\rm eff} (\widehat{T}_{s1}^{t+1} - \widehat{T}_{s2}^{t+1}) = 0 \tag{9}$$

In soil science, $K_{\rm eff} = \sqrt{K_{s1}K_{s2}}$ and $D_{Tl,\rm eff} = \sqrt{D_{Tl,s1}D_{Tl,s2}}$, since conductivity and diffusivity are assumed to be log-normally distributed. This modification applies to all the examples in this study, except for Section 3.4. With this modification, the mixed FEM scheme shares similarities with the finite volume method (FVM).

3. Transient spatial variations of soil properties and adaptive mesh refinement (Step B)

The baseline mixed FEM scheme is exploited under spatial variations of soil properties, especially the transient variations changing with



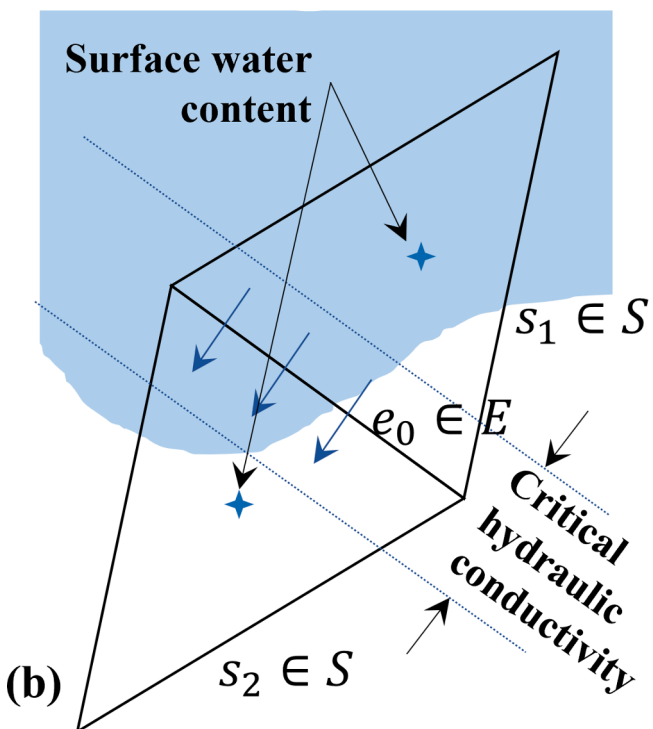


Fig. 3. Wetting front position relative to edge e_0 . (a) The wetting front is approaching from s_1 and roughly parallel to e_0 . There exists a neighborhood of e_0 containing dry soil, which forms a barrier for the liquid water flux. (b) The wetting front is approaching from s_1 but half of e_0 is included in the wet region. The water flux will be dominated by the wet portion of e_0 , which can be considered as a path for liquid water transfer.

respect to time. Tracing the spatial variations and adjusting the mesh size and the numerical scheme are the two critical components to ensure the simulation resolution and accuracy. Water infiltration is presented as the illustrative example, where relatively large soil water content differences in front of and behind the wetting front form a typical soil water

transfer problem with transient spatial variations of soil (hydraulic) properties (He and Ren, 2005; He and Ren, 2009; Li et al., 2016). However, the model proposed can be generalized to any other transient spatial variations of soil physical or chemical properties, such as temperature or chemical concentration in solute transfer. Soil heterogeneity can also be fitted into the model formulation by adding spatial positions (x,y) to the soil properties, e.g., changing K(h,T) to K(x,y,h,T). However, in this study, we emphasize transient variations of soil properties due to the instantaneous soil water and temperature regimes.

3.1. Localization of spatial variations of soil properties

When soil properties present relatively large spatial variabilities, such variabilities may not be fully captured by the baseline mixed FEM scheme, and incorrectly representing the spatial variabilities may induce computational errors (Luo et al., 2022). Moreover, handling transient variations of soil properties is challenging because the location and magnitude of such variations change with respect to time. Therefore, the soil property-of-interest (POI) and its distribution over the whole soil profile should be considered when constructing the mesh grid and establishing the mixed FEM scheme.

As a motivation example, Fig. 3 presents two possible relations between the triangular grid and the wetting front during water infiltration. The blue areas represent the high water content regions behind the wetting front. The white areas represent the low water content regions in front of the wetting front. Considering the liquid water flux across edge e_0 , in Fig. 3a, the high water content region stays in s_1 , and the wetting front does not reach e_0 . Thus, there exists a neighborhood of e_0 containing only dry soil, where the relatively low hydraulic conductivity limits the liquid water flux and creates a barrier to water infiltration. As the wetting front moves downwards and intersects with e_0 in Fig. 3b, a portion of e_0 with relatively high water content forms a path for liquid water flux from s_1 to s_2 . Comparing Fig. 3a and b, the soil water content in s_1 and s_2 , and the associated water potential gradient between s_1 and s_2 , may be similar. However, relatively large differences in liquid water fluxes across e_0 may occur.

Thus, solving the liquid water flux with the triangular grid in Fig. 3 may not achieve the optimum result, because in mixed FEM, each surface only has one soil water content value, and the sub-grid geometry of the wetting front is not recorded. To obtain a better numerical result, transient variations of soil properties (soil water content and hydraulic conductivity in this example) within individual surfaces should be considered. For the water infiltration example in Fig. 3, the transient variations should be described based on the wetting front location relative to e_0 (intersecting or roughly parallel), and the spatial resolution near the wetting front.

We define a gradient measure in Eq. (10) to trace the transient spatial variations of a given POI. Location with a relatively large gradient corresponds to the region where the POI has relatively high transient spatial variations.

$$\widetilde{\nabla}_{p} = \frac{\left| p_{si} - p_{sj} \right|}{\max p - \min p + \varepsilon}, \varepsilon > 0, s_{i}, s_{j} \in S$$
(10)

In Eq. (10), p is the POI (for example, $p = \theta$ in Fig. 3). p_{si} and p_{sj} are the POI values in two adjoined surfaces s_i and s_j . ε is a small positive number to avoid zero denominator. $\widetilde{\nabla}_p$ is not a typical gradient measure, for the denominator is not a distance value. That is because we focus on the relative magnitude of the stepwise differences of POI near the edge between s_i and s_i .

After computing $\widetilde{\nabla}_p$, a "k-means" clustering procedure assigns $\widetilde{\nabla}_p$ into two categories. The representative values for the "high $\widetilde{\nabla}_p$ " category and the "low $\widetilde{\nabla}_p$ " category, as well as the threshold between the two categories are determined via an iterative process (an instructive diagram of a "k-means" can be found in Fig. 9-3 and -4, Géron, 2019). "K-

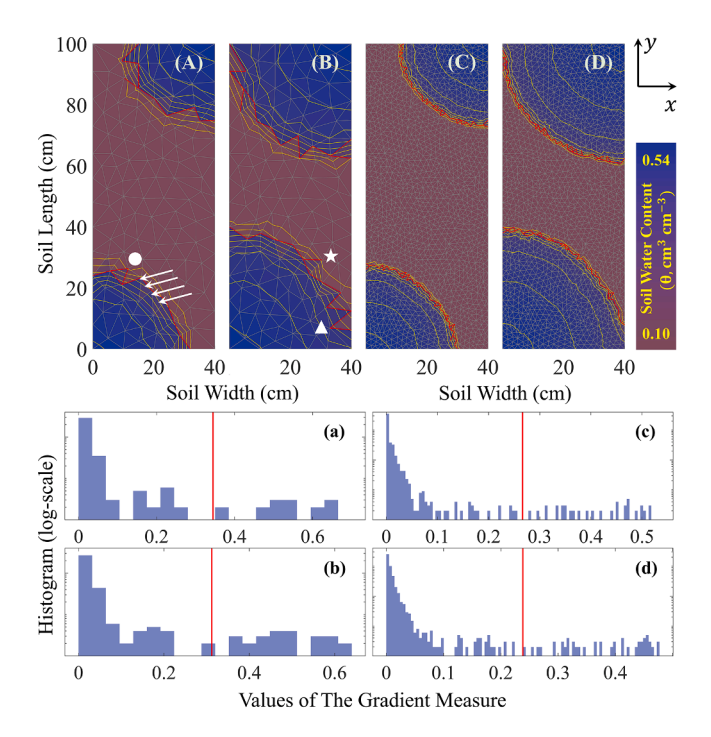


Fig. 4. Simulated soil water content under the imposed infiltration boundary conditions. (A) and (B) show the soil water content 3 h and 6 h after the infiltration started using the coarse grid. (C) and (D) show the soil water content simulated with the fine grid. (a-d) are the histograms of the gradient measure corresponding to (A-D), and the red vertical lines are the thresholds determined with "k-means". In (A-D), the yellow curves present the eight soil water content contours, which are $\theta=0.15,\,0.2,\,0.25,\,0.3,\,0.35,\,0.4,\,0.45$ and $0.5 \text{cm}^3 \text{ cm}^{-3}$. The red polylines present the approximations to the wetting fronts, which need additional polish to remove "dead ends" (\bigstar), "double connections" (\bullet) and "isolated triangles near the boundaries" (\bullet). The white arrows in (A) show the numerical fluctuations of soil water content near the wetting front in the coarse grid, where relatively high (darker blue) and relatively low (lighter blue) water content values alternate in adjoined surfaces. (For interpretation of the references to color in this figure legend, the reader is referred to the web version of this article.)

means" is an unsupervised learning method, so the $\widetilde{\nabla}_p$ data is the only required input.

The following numerical experiment emphasizes the necessity of considering transient spatial variations of soil properties and demonstrates the detection of the wetting fronts using the gradient measure and "k-means". Given a horizontally placed soil sample of 40 cm wide (x-axis) and 100 cm long (y-axis), with physical properties in Table 1. The initial water content and temperature are $\theta_{ini} = 0.1 \text{ cm}^3 \text{ cm}^{-3}$ and $T_{ini} = 25.0^{\circ}$ C. The boundaries are impermeable to heat flux. Water infiltration occurs at the two boundaries along the short side of the soil sample: along y = 0, the water infiltration flux is $q_{l,y=0}(x) = 5.0 \times$ $10^{-3}(x/40)^{10}\,\mathrm{cm\,s^{-1}}$; along y=100, the water infiltration flux is $q_{l,y=100}(x) = 5.0 \times 10^{-3} (1 - x/40)^{10} \,\mathrm{cm\,s^{-1}}$. Therefore, most of the infiltration occurs at the two opposite corners of the soil sample at (x =(0, y = 0) and (x = 40, y = 100). Numerical simulations are performed on a coarse triangular grid (229 surfaces, mesh size ≈ 10 cm) and a fine triangular grid (3084 surfaces, mesh size \approx 2 cm). The simulated soil water contents at 3 h and 6 h after the start of infiltration are shown in Fig. 4.

Different from the commonly studied uniform surface infiltration (He et al., 2005; He et al., 2006), water infiltration here is artificially created as a challenging example. More than one wetting front exists, and the wetting fronts are curved rather than straight lines with a uniform propagation speed. Using challenging examples is important for exploiting the model ability, while a simple uniform surface infiltration

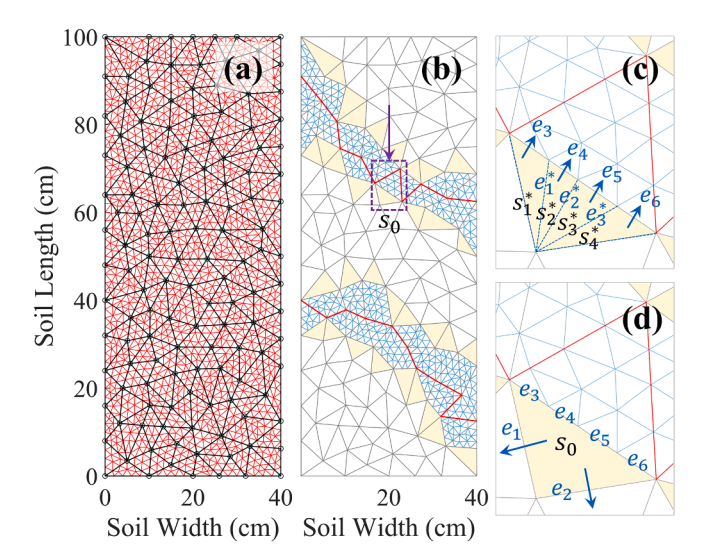


Fig. 5. Adaptive refinement of the mixed FEM grid and the "virtual-split" of the neighbor surfaces. (a) presents a coarse grid (black) and a nested fine grid (red). (b) presents a combined grid, based on the two (polished) approximations of wetting fronts (red) in Fig. 4B. The fine grid is invoked near the wetting front (blue), while the coarse grid is maintained for the rest regions. The neighbor surfaces are marked with yellow color. (c) and (d) present the "virtual-split" of a neighbor surface s_0 , when computing the fluxes between s_0 and fine surfaces (c), and when computing the fluxes between s_0 and adjoint coarse surfaces (d). (For interpretation of the references to color in this figure legend, the reader is referred to the web version of this article.)

example (with validation and performance analyses) is given in the supplementary material.

Fig. 4A and B present the soil water content distributions using the coarse triangular grid. Eight water content contours are shown, corresponding to $\theta=0.15,~0.2,~0.25,~0.3,~0.35,~0.4,~0.45$ and $0.5~{\rm cm}^3~{\rm cm}^{-3}$. Linear interpolations are used to estimate and plot the water content contours. Fig. 4C and D present the simulated soil water contents using the fine triangular grid. Multiple water content contours are concentrated nearby the two wetting fronts, indicating the rapid changes in soil water content. Moreover, the two wet regions in Fig. 4C and D are symmetric, and the wetting fronts have smooth arc shapes, which is reasonable based on the boundary conditions.

However, in Fig. 4A and B, because of the lack of sub-grid information for the soil water content, the contours near the wetting fronts cannot represent the geometry of the wetting fronts as well as the contours in Fig. 4C and D. Additionally, the contours in Fig. 4A and B are jagged due to the geometry of the underlying triangular grid. Numerical fluctuations of soil water content arise near the wetting fronts, where adjoined surfaces achieve high or low water contents alternately (see the surfaces pointed to by the white arrows in Fig. 4A). That is because the mixed FEM scheme strives to present rapid water content changes using coarse surfaces. Thus, based on the simulation in Fig. 4A and B, it is necessary to manipulate the mixed FEM scheme and the triangular grid to achieve a better presentation of the wetting fronts.

Histograms of the gradient measure for the soil water content distributions in Fig. 4A–D are shown in Fig. 4a–d, respectively. Most of the values are small, indicating relatively uniform soil water contents near those edges. The vertical lines in Fig. 4a–d are the thresholds determined with "k-means". Edges with gradient values larger than the thresholds are considered as the approximations to wetting fronts and colored red in Fig. 4A–D. In general, the red polylines match the wetting fronts. However, some errors exist, including "dead ends" (\bigstar), "double connections" (\bullet) and "isolated triangles near the boundaries" (\blacktriangle). Therefore, the red polylines need to be polished. The "dead ends" and the "isolated triangles" can be simply removed by a searching procedure. For the "double connections", the edges with the larger water content

gradients are selected. The polishing approach is similar to edge detection in image processing, especially the Canny filter (Canny, 1986). Examples of polished approximations to the wetting fronts are shown in Section 3.2 and Fig. 5b.

3.2. Adaptive mesh refinement

Based on the approximations to the wetting fronts, the mesh grid near the approximated wetting fronts should be refined to better represent the soil water regime. In the spatial grid, refinements can be different for each surface, such that performing mesh refinement via hierarchical iterations during simulations would lead to a slow computing speed [see the quad-tree graph method in Clément et al. (2021) or the computational cost for updating local transient variations in He and Ren (2009)]. An alternative way is to pre-define a fine grid and a coarse grid, where the fine grid is statically nested within the coarse grid. When local refinement is required, the fine grids in the refined regions are automatically invoked.

Fig. 5a presents an example of the nested grids, where the fine grid (red) serves as the refinement for the coarse grid (black). Fig. 5b presents the polished approximations (red polylines) to the wetting fronts in Fig. 4B, with "dead ends", "double connections" and "isolated triangles"

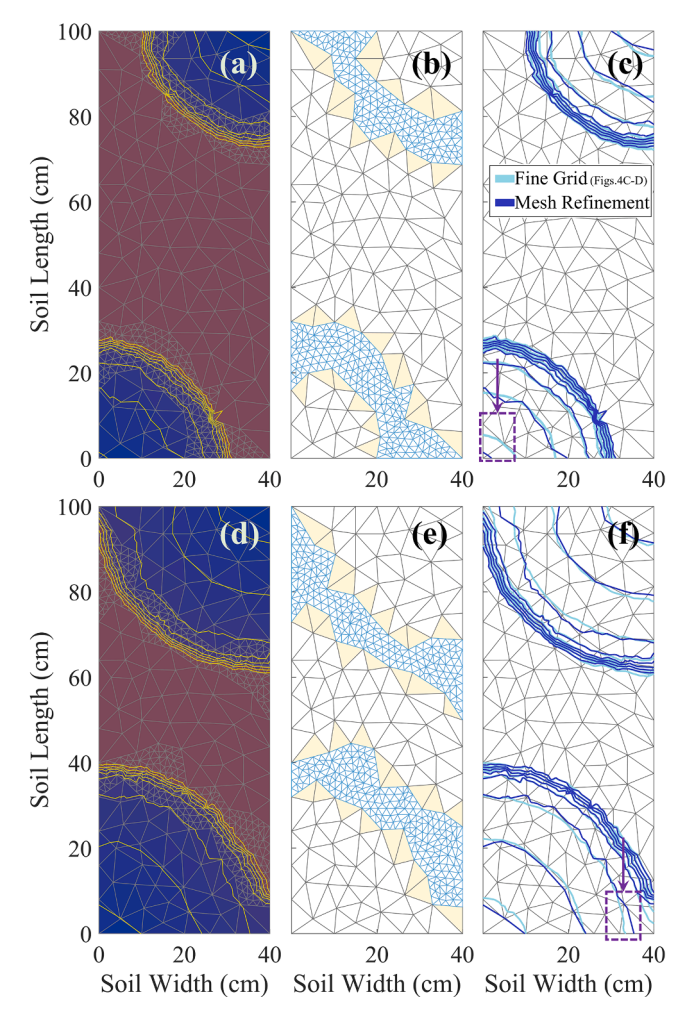


Fig. 6. Simulation results using the mixed FEM scheme with adaptive mesh refinement. (a) and (d) present the simulated soil water contents 3 h and 6 h after the onset of infiltration. (b) and (e) emphasize the refined regions (blue) and the "neighbor surfaces" (yellow). (c) and (f) compare the contours of the soil water content between the adaptively refined mesh and the fine mesh grid in Fig. 4C and D. (For interpretation of the references to color in this figure legend, the reader is referred to the web version of this article.)

removed. Local mesh refinement occurs in the coarse surfaces that share nodes or edges with the approximated wetting fronts. The fine grid in the refined regions (blue), plus the remaining portion of the coarse grid, form a combined grid based on the current water content distribution. Near the boundary of the soil sample, the refined region is expanded to ensure computational stability. The mixed FEM scheme can be applied to the combined grid, but modifications are needed for the yellow surfaces in Fig. 5b. The yellow surfaces are "neighbor surfaces", for they belong to the coarse grid but share at least one edge with the refined regions. From the perspective of finite element grid, the neighbor surfaces are no longer triangles but polygons. For example, the neighbor surfaces s_0 (yellow) demarcated with the purple rectangle in Fig. 5b has six edges, presented by e_k , $k=1,2,\cdots,6$ in Fig. 5c and d. Thus, a "virtual-split" of the neighbor surfaces is facilitated to ensure the triangularity of the mesh grid.

The idea of "virtual-split" is presented using s_0 in Fig. 5c and d. When computing the flux variables between the neighbor surface and the fine surfaces, s_0 is split into four segments (Fig. 5c) s_k^* , k=1,2,3,4, with three (interior) virtual edges e_k^* , k=1,2,3. The RT₀ basis function can be defined for each of the fine edges e_k , k=3,4,5,6, and the virtual edges e_k^* , k=1,2,3. In general, s_k^* 's do not belong to the fine grid but are temporarily created to facilitate the discretization of the flux variables in Eq. (4). When computing the flux variables between the neighbor surface and the coarse surfaces, s_0 is treated as one single surface (Fig. 5d). Therefore, in the combined grid, s_0 is thought to be split or unsplit, depending on which fluxes are computed. In addition, whether s_0 is split or not, s_0 and s_k^* , k=1,2,3,4, share the same soil water potential and temperature values. Thus, this procedure is called "virtual-split".

The mesh refinement is invoked automatically, and only relies on the instantaneous distribution of the POI (soil water content in this section). The regions that need to be refined follow the wetting fronts propagation. Hence, the mesh refinement procedure is called "adaptive mesh refinement".

The adaptive mesh refinement in the mixed FEM scheme is demonstrated as we redo the infiltration example in Section 3.1 using the two nested grids in Fig. 5. The simulated results are presented in Fig. 6, and the numerical performance is summarized in Table 2. The coarse and fine grids in Figs. 5 and 6 are the same ones in Fig. 4. But in Fig. 4, they are treated as two independent grids. Thus, the simulation results in Figs. 4 and 6 can be compared directly.

First, we provide a qualitative evaluation of the simulation results. Fig. 6a and d present soil water content 3 h and 6 h after the onset of infiltration. The combined grids are presented with gray triangles, and contours are shown in the same way as in Fig. 4. The adaptive mesh refinement near the wetting fronts and the neighboring surfaces are emphasized in Fig. 6b and e. The refined regions move automatically following the wetting fronts. The water content contours are emphasized in Fig. 6c and f. For comparison, the contours solved using the fine grid are also presented (see Fig. 4C and D). With adaptive mesh refinement, the contours are close to the wetting fronts and similar to the contours solved solely on the fine grid. This indicates the mesh refinement improves the accuracy of soil water content simulation near the wetting fronts.

Moreover, mesh refinement also affects the soil water contents outside of the refined regions. For example, as marked with the purple rectangle in Fig. 6f, the contour close to the refined region has a shape similar to the one in the fine grid (see Fig. 4D). However, the shape and locations of the contour in the purple rectangle in Fig. 6c are similar to the one in the coarse grid (see Fig. 4A) rather than to the corresponding contour in the fine grid. Therefore, the contours outside of, but near to, the refined regions, tend to receive benefits from the adaptive mesh refinement.

Second, we provide a quantitative evaluation for numerical performance. In Table 2, the fine grid soil water contents in Fig. 4C and D are assumed as the reference. The "Relative Error (Global)" represents the

Table 2Numerical performance of the water infiltration simulations using adaptive mesh refinement, coarse grid and fine grid.

Elapsed Time (h)	Number of Refined Surfaces †	Adaptive Mesh Refinement (Fig. 6a and d)		Coarse Grid (Fig. 4A and B)			Fine Grid (Fig. 4C and D)	
		Relative Error (Global) ‡	Relative Error (Local) §	Cumulative Computing Time (s) *	Relative Error (Global)	Relative Error (Local)	Cumulative Computing Time (s)	Cumulative Computing Time (s)
0	0/229	_	_	_	_	_	_	_
1	32/229	0.010	0.028	116	0.049	0.172	22	3459
2	37/229	0.014	0.033	272	0.049	0.172	37	5320
3	49/229	0.015	0.032	464	0.053	0.165	51	7141
4	55/229	0.016	0.034	671	0.058	0.185	66	8911
5	64/229	0.016	0.028	889	0.058	0.163	78	10,790
6	54/229	0.015	0.029	1114	0.049	0.179	92	12,774

- † The total number of coarse surfaces that need to be refined, relative to the total number of coarse surfaces (229 coarse surfaces).
- \ddagger The l_1 error of the simulated soil water content over the whole soil domain, relative to the fine grid simulation results.
- \S The l_1 error of the simulated soil water content within the refined regions (near the wetting fronts), relative to the fine grid simulation results.
- ** The hardware environments are Intel (R) Core (TM) i9-7900X CPU (with Turbo Boost off), a HyperX(R) Predator (TM) DDR4 RAM (3600 MHz, 32G) and an ASUS(R) Prime (TM) X299-Deluxe motherboard. The software environment is MATLAB R2021a. The max time step used in the Picard iteration is 5 s.

errors of simulated soil water contents in the mesh refinement or the coarse grid relative to the reference values for the whole soil sample, based on l_1 -norm. The "Relative Error (Local)" represents the same errors but only in the refined regions near the wetting fronts. With respect to elapsed time, the number of refined elements varies due to the change of the wetting front positions. The "Relative Error (Global)" and "Relative Error (Local)" of the mesh refinement results are about 1.5 % and 3 %, respectively, which are 1/3 and 1/6 of corresponding errors for the coarse grid results. To fulfill the adaptive mesh refinement, additional computing time is consumed compared to the coarse grid simulation. However, to achieve similar presentation of the wetting fronts, using adaptive mesh refinement still saves time compared to directly using the fine grid. In the simulations, the maximum time step in Picard iteration is restricted to 5 s, while in applications, such a restriction can be released for faster computing speed.

3.3. Additional remarks for the adaptive mesh refinement

To perform adaptive mesh refinement, POI is the only required information. The gradient measure, "k-means", and wetting front approximation are not based on soil physics but belong to machine learning methods. Therefore, the mixed FEM scheme with adaptive mesh refinement can be considered as a "learning-assisted process-based model".

Adaptive mesh refinement can be easily facilitated through the mixed FEM scheme, since the soil water content and temperature are computed on each surface rather than at each node in traditional FEM or FDM. In mesh refinement and "virtual-split", soil water content and temperature from the coarse surfaces can be directly assigned to the fine or virtual-split surfaces without computation. After mesh refinement, soil water content and temperature in the fine surfaces can be merged via weighted average and assigned back to the corresponding coarse surfaces. Such a simple procedure cannot be applied in traditional FEM or FDM because they focus on nodal values, where soil water content and soil temperature present linear or polynomial patterns in each surface depending on the choice of shape functions.

3.4. Discussion: Applying the wetting front approximations to upscaling model

Besides the adaptive mesh refinement, upscaling model is another method to conduct simulations with spatial heterogeneities. "Upscaling"

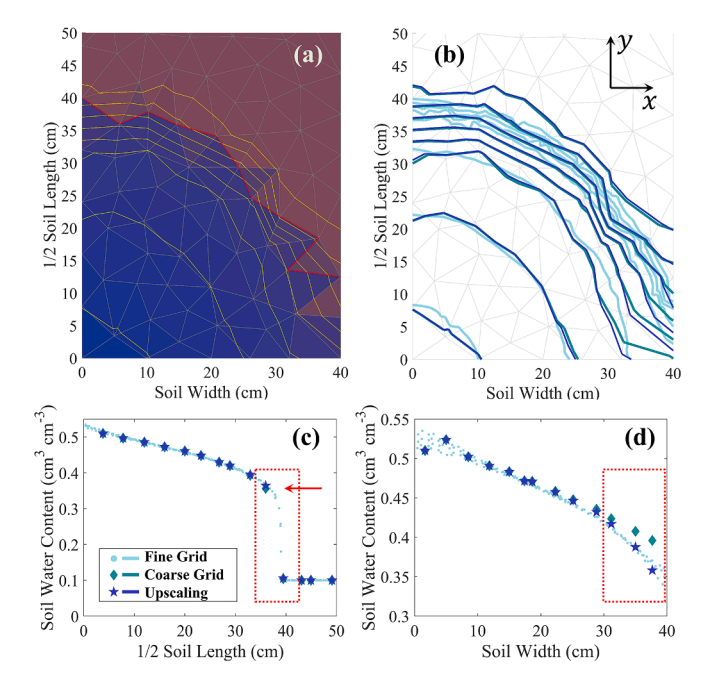


Fig. 7. Simulated water contents with the mixed FEM scheme in a coarse grid with upscaling. (a) presents the simulated water content 6 h after initiating the infiltration, with the upscaling model. (b) compares the water content contours in the coarse grid with or without upscaling, where the fine grid contours are shown as a reference. (c) and (d) compares the simulated soil water content for a 5 cm strip along the soil long side (x=0) and a 5 cm strip along the soil short side (y=0). Fluctuations in the fine grid results in (c) and (d) do not imply numerical oscillations but are due to the projection of the soil water content within the 5 cm strips onto the horizontal or vertical axes.

means adaptive estimation of the effective conductivity, diffusivity and capacity based on local soil information, which enhances numerical accuracy without mesh refinement (Hunter, 2004; Li et al., 2016). For the water infiltration example in Fig. 3, rather than using the geometric means in Eq. (9), the "effective" hydraulic conductivity at e_0 should be calculated in two ways to emphasize the water barrier in Fig. 3a and liquid water path in Fig. 3b.

$$\begin{cases} \text{Fig.3a}: \ K_{\text{eff}} = \frac{2}{1/K_{s1} + 1/K_{s2}} \sim \min(K_{s1}, K_{s2}) \text{ for } e_0 \\ \text{Fig.3b}: \ K_{\text{eff}} = \frac{1}{2}(K_{s1} + K_{s2}) \sim \max(K_{s1}, K_{s2}) \text{ for } e_0 \end{cases}$$

$$(11)$$

In Eq. (11), harmonic and algebraic means are used to determine the effective hydraulic conductivity, and " \sim " indicates the two sides are of the same order. To apply Eq. (11), we need to identify which edge is the barrier (similar to Fig. 3a), which edge serves as a path (similar to Fig. 3b), and which edge is far away from the wetting fronts such that the geometric mean in Eq. (9) can be used. This can be resolved with the wetting front approximation method in Section 3.1.

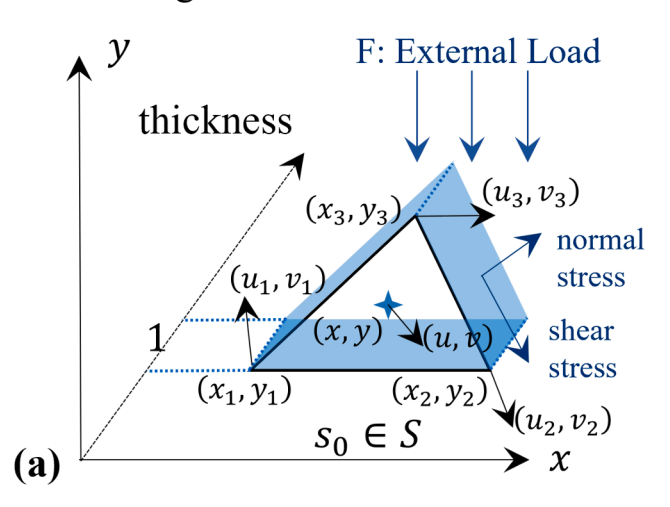
An example of the upscaling model is presented by repeating the previous water infiltration problem. Because of symmetry, only one half of the soil sample is presented in Fig. 7. Soil water transfer is simulated with three methods: "coarse grid with upscaling", "coarse grid without upscaling" [apply Eq. (9) for all edges], and "fine grid without upscaling". Fig. 7a presents the soil water content 6 h after initiating the infiltration, using coarse grid with upscaling. The yellow water content contours and the red wetting front are obtained in the same way as those in Figs. 4 and 6. Fig. 7b compares the water content contours among the three methods. Similar to the coarse grid results, the simulated contours with upscaling cannot provide sufficient geometrical details for the soil water distributions near the wetting fronts. However, as an advantage of the upscaling model, Fig. 7c and d present the simulated water contents for two 5 cm strips along x = 0 and y = 0, which shows the upscaling model improves the accuracy of the coarse grid water content, particularly near the wetting front demarcated by the red rectangles. The good matching between the upscaling results and the fine grid results can be easily observed in Fig. 7d. In Fig. 7c, the benefits are subtle. Nevertheless, the coarse grid result without upscaling, indicated by the red arrow, is slightly smaller than the other two simulation results. Therefore, compared to the adaptive mesh refinement, upscaling model is a "lightweight" method to use when accurate coarse-scale water contents are necessary, but the detailed geometry of the wetting fronts is not needed.

Throughout Step (B), when solving soil water content, the shapes and positions of the wetting fronts can be considered as global information, which means the information is based on the whole soil profile rather than one or two nearby surfaces in the mesh grid. Using global information is an ongoing and promising research topic in numerical PDEs with spatial heterogeneities (Chen et al., 2003; Durlofsky et al., 2007; Aarnes et al., 2008; Jiang et al., 2010).

4. Soil and mesh deformation (Step C)

The mesh deformation model for a deformable soil under an external load is presented, and it is prefixed to the mixed FEM scheme as an addon module. In geotechnical engineering, soil deformation and (saturated) water transfer are solved together since shallow or confined groundwater supports soil stress (Lewis and Schrefler, 1999). However, for agricultural soils, implementing soil deformation as a separate module is desirable. That is because (a) agricultural soils are noncompacted and unsaturated, where external load is mainly born by soil particles. (b) Soil deformation can be implemented as a "quasistatic" process (Xie and Leo, 2004; Zhang et al., 2021) and easily added to CHWT model without substantial changes of existing CHWT model structures. (c) Nonlinear interactions between soil deformation and CHWT exist. For example, the porosity change induced by soil deformation can perturbate soil water distribution, which inversely affects the soil effective stress (Fredlund et al., 2012). It is preferred to decouple those interactions and hence simplify the numerical computation. (d) Soil deformation model should be invoked or bypassed automatically based on the existence of an external load.

Configuration at t



Configuration at $t + \Delta t$

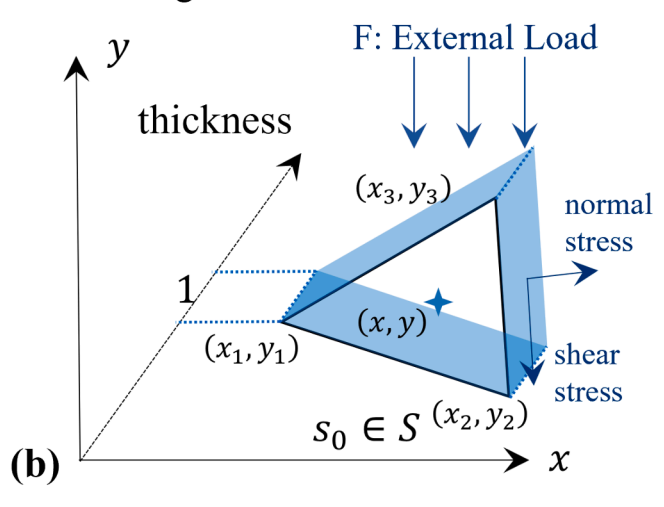


Fig. 8. Deformation of a triangular surface $s_0 \in S$ in a single time step under external load. For a 2D soil profile, a unit thickness (1cm, along the "virtual" third dimension) is assumed. The nodal coordinates $\left\{(x_i,y_i)\right\}_{i=1}^3$, nodal displacements $\left\{(u_i,v_i)\right\}_{i=1}^3$, and the coordinate (x,y) and displacement (u,v) for an arbitrary interior point are presented. F is the external load, which represents "force per unit length" in 2D space. Normal and shear stresses are only presented on one side, but they exist on all the edges. From t to $t+\Delta t$, s_0 is deformed and rotated from (a) to (b), which are represented by the nodal displacement $\left\{(u_i,v_i)\right\}_{i=1}^3$.

4.1. The soil deformation model

An updated Lagrangian formulation in Eq. (12) is adopted as the governing model from the current time step t to the next time step $t + \Delta t$, where summation convention with respect to i and j is assumed (Bathe, 2014).

$$\int_{t_{S}}^{t+\Delta t} \mathscr{S}_{ij} \, \delta^{t+\Delta t} \epsilon_{ij} \, d^{t} s =^{t+\Delta t} \delta \mathscr{R}$$
 (12)

 $^{t+\Delta t}_t \mathcal{S}_{ij} ({\rm N\,cm}^{-2})$ is the second Piola-Kirchhoff stress during the time interval $[t,t+\Delta t]$. $^{t+\Delta t}_t \epsilon_{ij}$ is the (dimensionless) Green-Lagrange strain. tS is the integral domain at time t, which can be either a single surface in the triangular grid or the whole soil profile Ω . δ represents the variation. $^{t+\Delta t}\delta\mathcal{B}({\rm J})$ is the virtual work from external load. Eq. (12) is originally written in 3D spaces in Bathe (2014). If 2D soil deformation is simulated, the unit of stress $^{t+\Delta t}_t \mathcal{S}_{ij}$ can be adjusted to N cm $^{-1}$, where we implicitly

assume the 2D soil profile have unit thickness along a "virtual" third dimension (see Fig. 8).

 $^{t+\Delta t}_t\mathcal{S}_{ij}$ and $^{t+\Delta t}_t\epsilon_{ij}$ in Eq. (12) can be linearized with the following incremental decompositions.

$$\int_{tS} \mathscr{C}_{ijrs} \, _{t}e_{rs} \, \delta_{t}e_{ij} \, d^{t}s + \int_{tS}^{t} \sigma_{ij} \, \delta_{t}\eta_{ij} \, d^{t}s = {}^{t+\Delta t} \delta \mathscr{R} - \int_{tS}^{t} \sigma_{ij} \, \delta_{t}e_{ij} \, d^{t}s$$

$$\text{where} \begin{cases} {}^{t+\Delta t} \mathscr{S}_{ij} = {}^{t}\sigma_{ij} + {}_{t}\mathscr{S}_{ij} = {}^{t}\sigma_{ij} + {}_{t}\mathscr{C}_{ijrs} \, _{t}e_{rs} \\ {}^{t+\Delta t} \varepsilon_{ij} = {}_{t}e_{ij} + {}_{t}\eta_{ij} = \underbrace{\frac{1}{2} \left(\frac{\partial_{t}u_{i}}{\partial x_{j}} + \frac{\partial_{t}u_{j}}{\partial x_{i}} \right)}_{{}^{t}e_{ij}} + \underbrace{\frac{1}{2} \frac{\partial_{t}u_{k}}{\partial x_{i}} \frac{\partial_{t}u_{k}}{\partial x_{j}}}_{{}^{t}\eta_{ij}} \end{cases}$$

$$(13)$$

 ${}^t\sigma_{ij}$ and ${}_t\mathscr{C}_{ijrs}$ are the Cauchy stress and the stress-strain constitutive tensor at time t. ${}_te_{ij}$ and ${}_t\eta_{ij}$ are the linear and nonlinear portions of ${}^{t+\Delta t}\varepsilon_{ij}$, expressed using the displacement u for each small segment in the soil profile. The subscripts i,j,k,r,s=1,2 represents the two coordinate axes for the 2D soil profile. Although ${}_t\eta_{ij}$ has a quadratic form, its variation δ ${}_t\eta_{ij}$ is linear because δ ${}_t\eta_{ij}=\frac{1}{2}\frac{\partial}{\partial x_i}\frac{\partial u_k}{\partial x_j}+\frac{1}{2}\frac{\partial}{\partial x_i}\frac{u_k}{\partial x_j}\frac{\partial}{\partial x_j}$, where u_k is the unknown and δu_k is an arbitrary virtual displacement.

Using FEM to solve 2D soil deformation, the goal of numerical discretization is to express the integrands in Eq. (13) with the nodal coordinates and displacements of a given triangular grid. Considering surface s_0 in Fig. 8a, the nodal coordinates and displacements are (x_i, y_i) and (u_i, v_i) , i = 1, 2, 3. Under the external load, s_0 is deformed and rotated to the position in Fig. 8b. The displacement (u, v) of an arbitrary point (x, y) in s_0 can be expressed using a "displacement-interpolation" relationship.

$$\begin{cases} u = a_u + b_u x + c_u y \\ v = a_v + b_v x + c_v y \end{cases}$$
 (14)

Nodal coordinates and displacements also satisfy Eq. (14). Hence, the coefficients (a_u, b_u, c_u) and (a_v, b_v, c_v) for s_0 can be obtained as in Eq. (15).

$$\begin{bmatrix} a_{u} \\ b_{u} \\ c_{u} \end{bmatrix} = \begin{bmatrix} 1 & x_{1} & y_{1} \\ 1 & x_{2} & y_{2} \\ 1 & x_{3} & y_{3} \end{bmatrix}^{-1} \begin{bmatrix} u_{1} \\ u_{2} \\ u_{3} \end{bmatrix} \stackrel{\text{def}}{=} \begin{bmatrix} A_{0}^{T} \\ A_{1}^{T} \\ A_{2}^{T} \end{bmatrix} \overrightarrow{U} \begin{bmatrix} a_{v} \\ b_{v} \\ c_{v} \end{bmatrix}$$

$$= \begin{bmatrix} 1 & x_{1} & y_{1} \\ 1 & x_{2} & y_{2} \\ 1 & x_{3} & y_{3} \end{bmatrix}^{-1} \begin{bmatrix} v_{1} \\ v_{2} \\ v_{3} \end{bmatrix} \stackrel{\text{def}}{=} \begin{bmatrix} A_{0}^{T} \\ A_{1}^{T} \\ A_{2}^{T} \end{bmatrix} \overrightarrow{V}$$

$$(15)$$

With the vectors $A_0, A_1, A_2, \overrightarrow{U}$, and \overrightarrow{V} defined in Eq. (15), spatial derivatives in Eq. (13) can be expressed using the nodal displacement.

$$\frac{\partial u}{\partial x} = b_u = A_1^T \overrightarrow{U}; \frac{\partial u}{\partial y} = c_u = A_2^T \overrightarrow{U}
\frac{\partial v}{\partial x} = b_v = A_1^T \overrightarrow{V}; \frac{\partial v}{\partial y} = c_v = A_2^T \overrightarrow{V}$$
(16)

Therefore, the linear and nonlinear portions of ${}^{t+\Delta t}_{t} \in_{ij}$, namely ${}^{t}e_{ij}$ and ${}^{t}\eta_{ij}$, can then be rewritten using Eq. (16) as the following "displacement–strain" relationship.

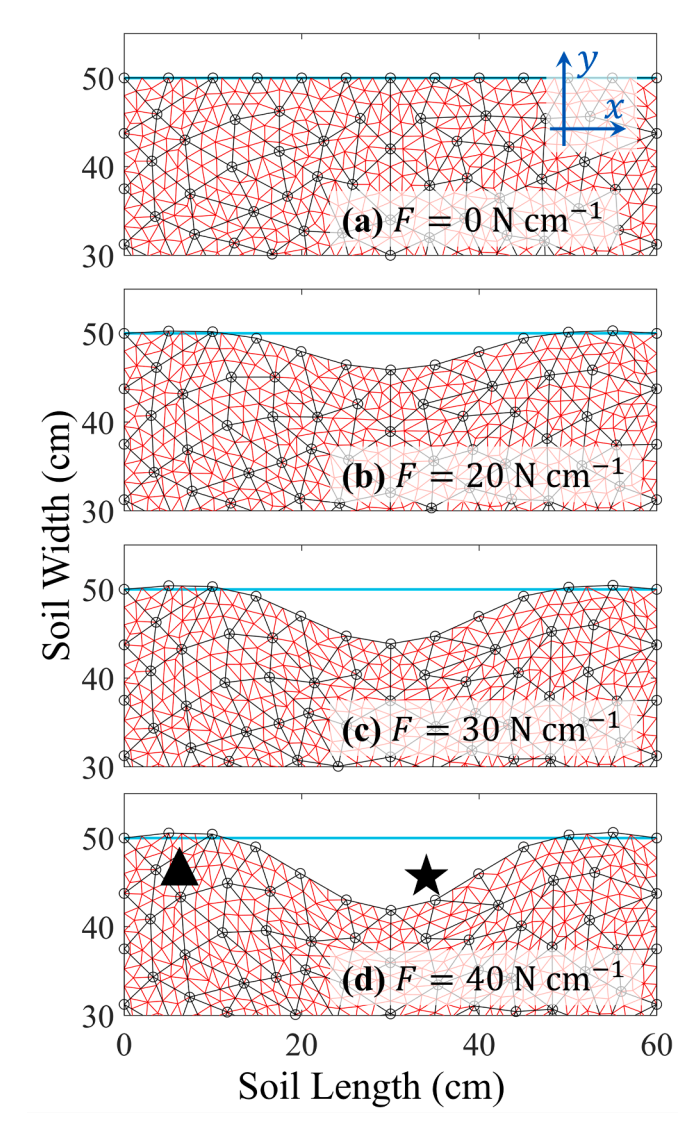


Fig. 9. The original soil (a) and the deformed soil under the external loads $F = 20 \,\mathrm{N\,cm^{-1}}(b)$, $F = 30 \,\mathrm{N\,cm^{-1}}(c)$ and $F = 40 \,\mathrm{N\,cm^{-1}}(d)$, applied between $x = 20 \,\mathrm{cm}$ and $x = 40 \,\mathrm{cm}$. The cyan lines indicate the original soil surface, the black lines and circles indicate the coarse grid edges and nodes, and the red lines indicate the fine grid edges. In (d), \star denotes the compacted region under the external load, and \blacktriangle denotes the uplifts outside of the loading region. (For interpretation of the references to color in this figure legend, the reader is referred to the web version of this article.)

$${}_{t}e_{11} = A_{1}^{T}\overrightarrow{U}; \ {}_{t}e_{12} = \ {}_{t}e_{21} = \frac{1}{2} \left(A_{2}^{T}\overrightarrow{U} + A_{1}^{T}\overrightarrow{V} \right); \ {}_{t}e_{22} = A_{2}^{T}\overrightarrow{V}$$

$${}_{t}\eta_{11} = \frac{1}{2} \left(\overrightarrow{U}^{T} A_{1} A_{1}^{T} \overrightarrow{U} + \overrightarrow{V}^{T} A_{1} A_{1}^{T} \overrightarrow{V} \right); \ {}_{t}\eta_{12} = \frac{1}{2} \left(\overrightarrow{U}^{T} A_{1} A_{2}^{T} \overrightarrow{U} + \overrightarrow{V}^{T} A_{1} A_{2}^{T} \overrightarrow{V} \right)$$

$${}_{t}\eta_{21} = \frac{1}{2} \left(\overrightarrow{U}^{T} A_{2} A_{1}^{T} \overrightarrow{U} + \overrightarrow{V}^{T} A_{2} A_{1}^{T} \overrightarrow{V} \right); \ {}_{t}\eta_{22} = \frac{1}{2} \left(\overrightarrow{U}^{T} A_{2} A_{2}^{T} \overrightarrow{U} + \overrightarrow{V}^{T} A_{2} A_{2}^{T} \overrightarrow{V} \right)$$

$$(17)$$

From Eq. (17), the variations $\delta_t e_{ij}$ and $\delta_t \eta_{ij}$ can be derived using the chain rule and product rule.

$$\delta_{i} e_{11} = A_{1}^{T} \delta \overrightarrow{U}; \delta_{i} e_{12} = \delta_{i} e_{21} = \frac{1}{2} \left(A_{2}^{T} \delta \overrightarrow{U} + A_{1}^{T} \delta \overrightarrow{V} \right); \delta_{i} e_{22} = A_{2}^{T} \delta \overrightarrow{V}$$

$$\delta_{i} \eta_{11} = \delta \overrightarrow{U}^{T} A_{1} A_{1}^{T} \overrightarrow{U} + \delta \overrightarrow{V}^{T} A_{1} A_{1}^{T} \overrightarrow{V}; \delta_{i} \eta_{12} = \frac{1}{2} \left(\delta \overrightarrow{U}^{T} A_{1} A_{2}^{T} \overrightarrow{U} + \delta \overrightarrow{V}^{T} A_{1} A_{2}^{T} \overrightarrow{U} + \delta \overrightarrow{V}^{T} A_{2} A_{1}^{T} \overrightarrow{U} + \delta \overrightarrow{V}^{T} A_{2} A_{1}^{T} \overrightarrow{V} \right)$$

$$\delta_{i} \eta_{21} = \frac{1}{2} \left(\delta \overrightarrow{U}^{T} A_{2} A_{1}^{T} \overrightarrow{U} + \delta \overrightarrow{V}^{T} A_{2} A_{1}^{T} \overrightarrow{V} + \delta \overrightarrow{U}^{T} A_{1} A_{2}^{T} \overrightarrow{U} + \delta \overrightarrow{V}^{T} A_{1} A_{2}^{T} \overrightarrow{V} \right); \delta_{i} \eta_{22} = \delta \overrightarrow{U}^{T} A_{2} A_{2}^{T} \overrightarrow{U} + \delta \overrightarrow{V}^{T} A_{2} A_{1}^{T} \overrightarrow{V} \right)$$

$$(18)$$

Expanding Eqs. (14)–(18) to the whole triangular grid, Eq. (13) can be written using \overrightarrow{U} , \overrightarrow{V} , $\delta \overrightarrow{U}$ and $\delta \overrightarrow{V}$ [see Table 6.4 in Bathe, 2014, and Eqs. (10)–(12) in Yuan et al., 2019, for the definition of the interpolation

Under the "quasi-static" assumption, we simply assume the stress rate of σ^J is constant, such that the change of σ^J in Δt can be written as $\Delta \sigma^J$. $_t\omega$ is the skew-symmetric spin tensor. $c_i, i=1,2,3,4$ are (dimensionless) empirical parameters. Based on Eqs. (13) and (17), $_te$ and $_t\omega$ have the following matrix forms.

$${}_{l}e_{ij} \stackrel{\text{def}}{=} \frac{1}{2} \left(\frac{\partial {}_{l}u_{i}}{\partial x_{j}} + \frac{\partial {}_{l}u_{j}}{\partial x_{i}} \right) \Rightarrow {}_{l}e = \frac{1}{2} \begin{bmatrix} 2A_{1}^{T}\overrightarrow{U} & A_{2}^{T}\overrightarrow{U} + A_{1}^{T}\overrightarrow{V} \\ A_{1}^{T}\overrightarrow{V} + A_{2}^{T}\overrightarrow{U} & 2A_{2}^{T}\overrightarrow{V} \end{bmatrix} {}_{l}\omega_{ij} \stackrel{\text{def}}{=} \frac{1}{2} \left(\frac{\partial {}_{l}u_{i}}{\partial x_{j}} - \frac{\partial {}_{l}u_{j}}{\partial x_{i}} \right) \Rightarrow {}_{l}\omega = \frac{1}{2} \begin{bmatrix} 0 & A_{2}^{T}\overrightarrow{U} - A_{1}^{T}\overrightarrow{V} \\ A_{1}^{T}\overrightarrow{V} - A_{2}^{T}\overrightarrow{U} & 0 \end{bmatrix}$$

$$(21)$$

matrix in Eq. (19)]. In Eq. (19), \overrightarrow{U} , \overrightarrow{V} , $\delta \overrightarrow{U}$ and $\delta \overrightarrow{V}$ are the displacements and virtual displacements of all the nodes, and Ω represents the whole soil profile.

$$\underbrace{\left[\delta \overrightarrow{U}^{T}, \delta \overrightarrow{V}^{T}\right] \left[\int_{\iota_{\Omega}} B_{L}^{T} \mathscr{C} B_{L} d^{t} s\right] \left[\frac{\overrightarrow{U}}{\overrightarrow{V}}\right]}_{\sim \int_{\iota_{S}} \iota \mathscr{C}_{ijrs} \ \iota e_{rs} \ \delta_{i} e_{ij} \ d^{t} s} + \underbrace{\left[\delta \overrightarrow{U}^{T}, \delta \overrightarrow{V}^{T}\right] \left[\int_{\iota_{\Omega}} B_{NL}^{T} {}^{t} \sigma B_{NL} d^{t} s\right] \left[\frac{\overrightarrow{U}}{\overrightarrow{V}}\right]}_{\sim \int_{\iota_{S}} \sigma_{ij} \ \delta_{i} \eta_{ij} \ d^{t} s} + \underbrace{\left[\delta \overrightarrow{U}^{T}, \delta \overrightarrow{V}^{T}\right] \left[\int_{\iota_{\Omega}} B_{NL}^{T} {}^{t} \sigma d^{t} s\right]}_{\sim \int_{\iota_{S}} \sigma_{ij} \ \delta_{i} e_{ij} \ d^{t} s} \tag{19}$$

Each term in Eq. (19) corresponds to one integral in Eq. (13) marked under the integrals. The principle of virtual work implies that Eq. (19) must be satisfied for arbitrary $\delta \overrightarrow{U}$ and $\delta \overrightarrow{V}$. Thus, Eq. (19) is essentially a linear system for the nodal displacements \overrightarrow{U} and \overrightarrow{V} , which are directly related to the mesh deformation.

 $_t$ \mathcal{C}_{ijrs} $_t$ $_t$ $_t$ $_t$ is the incremental of Cauchy stress from $_t$ to $_t$ + $_t$ $_t$ In this study, it is expressed with a hypoplastic model, where a simple mathematical equation can approximate the stress–strain constitutive relations, and the separation of elastic and plastic portions in the traditional method is not required (Wang and Wu, 2011; Peng et al., 2015). The stress–strain constitutive relation for $_t$ $_t$ $_t$ is expressed as follows.

Therefore, the hypoplastic model in Eq. (20) can be implemented in the discretized formulation in Eq. (19), because all the terms in Eq. (20) are written in the nodal displacement as shown in Eq. (21).

4.2. Illustrative example

Soil deformation induces two effects on CHWT simulations. (a) Local soil bulk density and water content may change in the deformed regions. For example, when surface soil is consolidated, the volume of the shallow soil decreases, such that the volumetric water content will increase even if there is no water transfer. (b) Deformation alters the local soil properties, especially the hydraulic properties, due to changes in local porosity and connectivity.

For (a), soil water content is changed inversely proportional to the soil volume, and we assume that deformation does not induce soil temperature changes in this study. However, (b) is challenging due to the lack of systematic constitutive relations for soil hydraulic and thermal properties. In this study, the following assumptions are adopted. First, the soil water characteristic curve and the soil saturated hydraulic conductivity follows the von Genuchten type equation in Tian et al. (2019).

$$\theta = \rho_b \theta_{ro} + \left[\frac{\rho_s - \rho_b}{\rho_s - \rho_{bo}} \theta_{so} - \rho_b \theta_{ro} \right] \times \left[\frac{1}{1 + (\rho_b^{-3.97} \alpha_0 |h|)^n} \right]^{1 - 1/n}$$

$$K_s = K_{so} \left[\frac{\rho_s - \rho_b}{\rho_s - \rho_{bo}} \theta_{so} - \rho_b \theta_{ro} \right]^{2.5} \times \rho_b^{-7.96}$$
(22)

$${}_{t}\mathscr{C}_{ijrs} {}_{t}e_{rs} = \Delta {}_{t}\sigma = {}_{t}\omega {}_{t}\sigma + {}_{t}\sigma {}_{t}\omega^{T} + \underbrace{c_{1}\mathrm{Tr}({}_{t}\sigma) {}_{t}e + c_{2}\mathrm{Tr}({}_{t}e) {}^{t}\sigma + c_{3}\frac{\mathrm{Tr}({}^{t}\sigma_{t}e)}{\mathrm{Tr}({}^{t}\sigma)}\sigma + c_{4}({}^{t}\sigma + {}^{t}\sigma^{*})\| {}_{t}e\| \Delta\sigma^{J}$$

$$\underbrace{\Delta\sigma^{J}}_{eff}$$

In general, Eq. (20) should be written using the time differentiation of ${}^t\sigma$, for the Jaumann stress σ^J is usually expressed as a stress rate.

In Eq. (22), θ_{so} and θ_{ro} (cm³ cm⁻³) are the original saturated and residue soil water content, where "original" indicates the soil before any

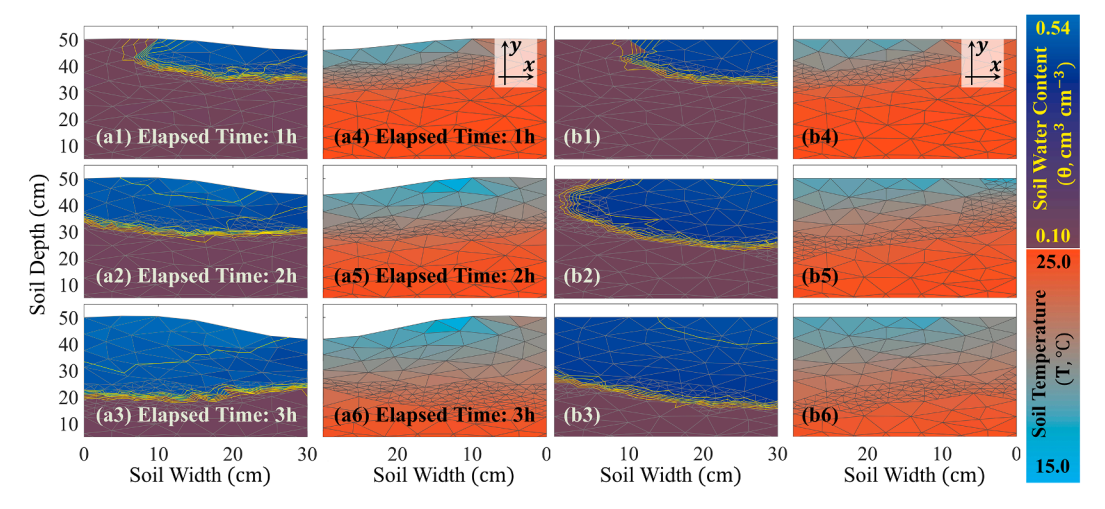


Fig. 10. Simulated soil water content and soil temperature regimes 1 h (the first row), 2 h (the second row) and 3 h (the third row) after initiating the infiltration for the deformed soil (a) and the non-deformed soil (b), respectively. Soil deformation due to the external loads applied or increased at 0.5 h, 1.5 h and 2.5 h are presented by the shapes of the soil surface. The CHWT simulations are performed for both deformed soil (under the external load) and the non-deformed soil (without the external load), such that the effects of soil deformation on soil water and temperature regimes can be presented.

deformation. $\rho_s \approx 2.65 ({\rm g~cm^{-3}})$ is the soil particle density, $\rho_{bo} ({\rm g~cm^{-3}})$ is the original soil bulk density, n and α_0 are coefficients depending on the soil type, $K_{so} ({\rm cm~s^{-1}})$ is the original soil saturated hydraulic conductivity. Second, the soil thermal conductivity follows a Kozeny-Carman type equation (Côté and Konrad, 2005).

$$\lambda_s = \lambda_{so}^{1-\phi} \times 0.6^{\phi} \tag{23}$$

 $\lambda_{so}(W\,cm^{-1}\,K^{-1})$ is the original thermal conductivity at the saturated soil water content, and ϕ is the soil porosity. In this study, λ_{so} is equal to $\lambda(\theta=\theta_s)$ in Table 1, and then the actual thermal conductivity can be computed using λ_s and θ . Third, we assume the vapor diffusivity, as well as the related latent heat transfer, vary proportionally with respect to soil porosity during deformation. These assumptions may not necessarily represent real-world conditions, but they enable us to illustrate the model architecture.

An idealized water infiltration experiment is presented to illustrate the concatenation of the soil deformation module and the CHWT model. In surface infiltration measurements, the infiltrometer not only supplies liquid water flux, but also acts as an external load at soil surface (Mohanty et al., 1994; Ankeny et al., 1988; Luo et al., 2019), especially when the shallow soil profile is recently tilled (Nishiwaki and Horton, 2020). Therefore, soil deformation should be considered to correctly interpret the infiltration experiments. This is a synthetic example, where external load is emphasized, and temperature boundary conditions are also included to fulfill a complete CHWT problem.

A vertically placed soil sample of 60 cm wide (x-axis) and 50 cm deep (y-axis) is considered in this example. The soil physical properties are listed in Table 1, but the soil water characteristic curve, hydraulic conductivity and thermal conductivity are substituted by Eqs. (22) and (23), with $\theta_{ro}=0.02 \, ({\rm cm}^3 \, {\rm cm}^{-3})$, $\alpha_0=0.027$, and n=1.3. The initial water content and temperature are $\theta_{ini}=0.1 \, {\rm cm}^3 \, {\rm cm}^{-3}$ and $T_{ini}=25 \, ^{\circ} \, {\rm C}$. The boundaries along the vertical side (x=0, x=60) are impermeable to heat and water fluxes. The soil bottom (y=0) is impermeable to water flux but has a constant temperature of $25 \, ^{\circ} \, {\rm C}$. On the soil surface (y=50), a constant temperature of $15 \, ^{\circ} \, {\rm C}$ is assumed and liquid water infiltration $q_1=1.0 \times 10^{-3} \, {\rm cm} \, {\rm s}^{-1}$ occurs between x=20 and x=40.

A 3-hour CHWT simulation of water infiltration is performed. At 0.5 h, soil surface receives an external load of $F=20~{\rm N~cm^{-1}}$ between $x=20~{\rm and}~x=40$. Then, the external load is increased by $10~{\rm N~cm^{-1}}$ twice at 1.5 h and 2.5 h after the simulation onset. Thus, the soil sample is deformed three times. The (dimensionless) empirical parameters in Eq. (20) are $c_1\approx -43$, $c_2\approx -430$, $c_3\approx -184$, and $c_4\approx -120$ (those values

are averaged from Tables 3.8 and 3.10 in Wang and Wu, 2009). The external load is assumed to be the only driving force for soil deformation, and gravity is considered in liquid water flux. As a comparison, the infiltration simulation is also performed for soil without external load, such that the effects of soil deformation on soil water and temperature regimes can be presented.

Fig. 9 presents the original and the deformed soil grids. The coarse grid is colored black, and the fine grid is colored red. The magnitude of soil deformation increases with respect to the external load. Compared to Fig. 9a, the maximum compaction ratios in Fig. 9b-d are 0.93, 0.89 and 0.84. Because the external load is only applied on the middle 1/3 of the whole soil surface, a concave furrow is formed in that region and marked with \star (Fig. 9d). In addition, the compaction pressure will not only transfer vertically under the loading region, but also transfer laterally. Therefore, small uplifts occur outside the loading region and marked with \star (Fig. 9d).

The simulated soil water content and temperature 1 h, 2 h, and 3 h after initiating the infiltration are presented in Fig. 10. Due to symmetry, only half of the soil sample is included. Since the external load is applied or increased at 0.5 h, 1.5 h and 2.5 h, soil in Fig. 10a1–a6 can represent soil deformation after the application and increasing of the external load, while Fig. 10b1–b6 present soil water content and temperature without deformation. The water content contours are presented in the same way as those in Figs. 5, 7 and 8. As time evolves, for both deformed and non-deformed soils, the wetting front propagates, and the cold region expands in the soil due to the relatively low surface temperature at y=50.

When soil deformation occurs, the hydraulic conductivity near the compressed portion decreases. Therefore, although the infiltration is applied between x=20 and x=40, soil water tends to redistribute laterally rather than transfer downwards. As a result, deep percolation of the wetting fronts occurs near $x\approx 10$ in Fig. 10a1–a3, while at x=30, the wetting fronts stay at relatively shallow positions. However, for the simulated soil water content in non-deformed soil, rapid propagation of the wetting fronts occurs near $x\approx 30$ in Fig. 10b1–b3, right under the surface where infiltration is applied. Thus, the water content contours near the wetting fronts follow different patterns between Fig. 10a1–a3 and Fig. 10b1–b3, and such differences in soil water transfer also induce variations in soil temperature regimes between Fig. 10a4–a6 and Fig. 10b4–b6.

Moreover, due to soil compression, relatively high soil water content is achieved in the deformed soil in Fig. 10a1-a3, compared to the non-deformed soil in Fig. 10b1-b3. In Fig. 10a1-a3, a relatively large

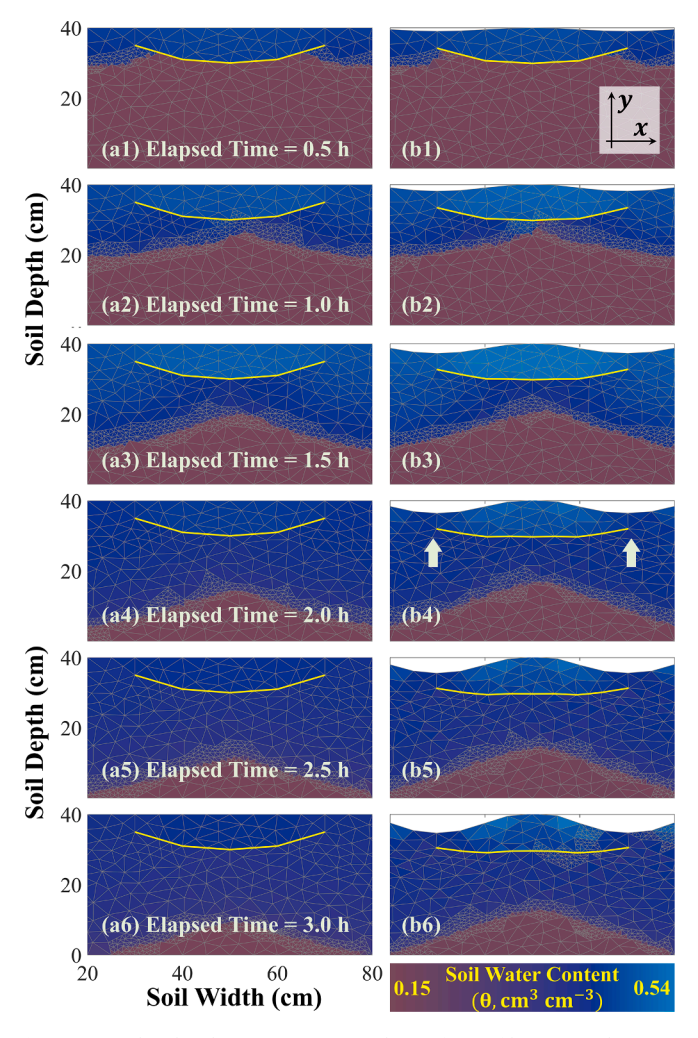


Fig. 11. Simulated soil water contents under surface infiltration with no surface compaction (column a) or with nonuniform surface compaction (column b). In each column, 6 figures present soil water distribution for every 0.5 h. Surface infiltration only lasts for 1.5 h, so the figures a4-a6 and b4-b6 present soil water redistributions without infiltration. The elapsed time since the initiation of the simulation is presented for each row. Local mesh refinements are presented by the gray mesh grid.

contrast gradient is used between cyan and dark blue to exaggerate the soil water content variations in the deformed regions behind the wetting fronts, and hence a relatively large color difference does not imply a big change in soil water content.

4.3. Additional remarks for the soil deformation model

Incorporating soil deformation emphasizes the flexibility of adaptive mesh refinement, where local mesh refinement can be performed with moving mesh grids (Fig. 10). As an advantage of the mixed FEM scheme, during soil deformation, water and heat are conserved in individual surfaces of the triangular grid and moved together with the surfaces following the deformation pattern. Therefore, there is no need to compute the convective coordinate changes of water and temperature. In other words, the motion of soil matrix, soil water and soil heat during deformation can be treated solely based on the Lagrange perspective. However, the influence of soil pore water on soil effective stress (the negative pressure from the meniscus) is not included.

In the illustrative example, assumptions are made for soil hydraulic and thermal properties under deformation. Obtaining valid systematic constitutive relations for soil hydraulic and thermal properties is an open and challenging topic in soil physics because of the following reasons. First, the constitutive relations, such as Eqs. (22) and (23), are from separate (experimental) studies. When coupling Eqs. (22) and (23) in one numerical model, their consistency, compatibility and performance are not fully validated. Second, the constitutive relations are measured under static and uniform soil bulk densities. However, during soil deformation, soil bulk density changes dynamically and may not be uniform. Moreover, the constitutive relations should not only include soil bulk density and porosity as independent variables but also include the soil deformation history, since soil deformation is irreversible. For example, given a soil sample with initial bulk density ρ_{b0} and porosity ϕ_0 , it can be compacted to the final density ρ_{bt} and porosity ϕ_t suddenly or gradually. The final soil hydraulic and thermal properties under the two compaction methods may not be the same.

Even though valid systematic constitutive relations are not fully established, it is still meaningful to develop the model framework in this study. New constitutive relations of soil hydraulic and thermal properties can be simply incorporated in this model framework, and this model framework can serve as a platform to test future constitutive relations.

4.4. Additional remarks for the difference between model development and model application

Up to this point, the three model construction steps are complete. We start with the mixed FEM scheme and follow by including spatial variations of soil properties and soil deformation. Illustrative examples are designed to emphasize the accomplishments of individual steps. For model applications, we follow a reversed procedure. (a) In each time step, we first determine soil deformation based on external loads. If soil deformation occurs, the mesh grid is reshaped and the soil water content or porosity in the deformed regions are recomputed. (b) Local mesh refinement is performed if needed based on the spatial variations of soil properties, especially the soil water content in this study. (c) Finally, simulation of CHWT with the mixed FEM scheme is conducted in that time step.

5. Simulating coupled heat and water transfer in soil with subsurface membranes: An application example

We present a potential application example to demonstrate the entire model framework. Subsurface membranes can perform a range of functions in agriculture and civil engineering. For example, in road foundation, a cup-shaped subsurface membrane can concentrate water and encourage drainage to stabilize surface pavement (see the J-Drain webpage https://www.j-drain.com/edge-drain.html). In arid regions, a buried double-layered membrane with holes can be designed as a "water vapor diode", which traps water vapor near the double-layered membrane (see Fig. 1 in Wang et al., 2017). One recent application of subsurface membranes is the SWRT (subsurface water retention technology, Guber et al., 2015), where a "bowl-shape" membrane is placed under plant roots to partially reduce the deep percolation of soil water and improve the root zone water storage. A simple version of SWRT is presented as the application example, with the "bowl-shape" membrane shown in Fig. 11.

From the water management perspective, immediate questions for SWRT are (a) how it affects soil heat and water redistributions, (b) how much water can be preserved, and (c) when surface soil is compacted such that the membrane loses its geometrical shape during soil deformation, whether the membrane can maintain its function to preserve water. From the modeling perspective, the subsurface membrane creates two challenges. (a) It is an interior boundary that perturbates water and heat fluxes. For example, during infiltration, even if the infiltration flux is uniform on the soil surface, the "bowl-shape" membrane can fragment the wetting front into multiple pieces and affect the soil water distribution. (b) Under surface compaction, soil near the membrane could be deformed such that the shape of the membrane and its effects on soil heat and water transfer could change. Moreover, evaluating soil water

management under (long-term and slow) soil deformation is rarely studied. Thus, from both practical and modeling perspectives, SWRT with subsurface membrane not only provides a proper example to demonstrate the model applications, but also implies future research on the long-term stability of soil water management.

In this example, consider a vertically placed soil sample of 100 cm wide (x-axis) and 40 cm deep (y-axis) in Fig. 11a1. The initial soil water content and temperature are $0.15~{\rm cm^3~cm^{-3}}$ and 25° C. The boundaries in the vertical direction (x=0,x=100) are impermeable to heat and water fluxes. The soil bottom (y=0) is impermeable to water flux. The SWRT "bowl-shape" membrane placed near the soil surface (yellow) blocks the liquid water and water vapor fluxes but exerts no effects on conductive heat transfer. Soil physical properties are the same as the example in Section 4.2.

Liquid water fluxes are modeled with a 3-hour simulation. In the first 1.5 h, liquid water infiltration $q_l=0.75\times 10^{-3}~{\rm cm\,s^{-1}}$ is uniformly placed on the soil surface (y=40), and after that, the soil surface is impermeable to water flux. Temperatures at the two horizontal boundaries (y=0,y=40) are 25° C. In one case, soil deformation is not included, corresponding to the SWRT design in Guber et al. (2015). In the other case, 15 min after the simulation launched, soil surface receives an external load of $F=5~{\rm N~cm^{-1}}$ in $x\in[20,40]$ and $x\in[60,80]$, and for every 0.5 h, the load is increased by $5~{\rm N~cm^{-1}}$ with the terminal value equal to $F=30~{\rm N~cm^{-1}}$. In that way, interrow traffic compaction can be approximated with a ridge forming near the planting row at (x=50,y=40). Thus, the geometrical configuration and the water storage above the "bowl-shape" membrane with or without soil compaction are compared.

The simulated soil water contents for each 0.5 h are shown in Fig. 11, where the left column (Fig. 11a) presents the classical SWRT without soil deformation, and the right column (Fig. 11b) presents the SWRT under surface compaction. First, the wetting fronts are successfully traced by the adaptive mesh refinement. For example, 0.5 h after the initiation of the infiltration (Fig. 11a1 and b1), the wetting fronts are fragmented by the "bowl-shape" membrane, and each piece is associated with an individual refined region. As the infiltration proceeds, the fragmented wetting fronts bypass the membrane and merge below the membrane (Fig. 11a2, a3, b2 and b3). In Guber et al. (2015), HYDRUS-2D uses relatively fine grids near the "bowl-shape" membrane to depict the geometry of the subsurface membrane (see Fig. 3 in their paper), while the adaptive mesh refinement uses a fine grid to provide detailed soil water dynamics. Even close to the "bowl-shape" membrane, if the soil water content is uniform, using a fine mesh grid is unnecessary. However, far away from the "bowl-shape" membrane, if the soil water content is rapidly fluctuating (near the wetting front), it is necessary to invoke the fine mesh grid to reveal the small-scale soil water distributions. Second, even though surface compaction deforms the membrane, soil water content above the membrane still increases during the infiltration period, for the dominant liquid water flux is downward and the deformed membrane can intercept the liquid water flux. Third, with or without surface compaction, after the 1.5 h of infiltration, the water stored above the membrane decreases (Fig. 11a4-a6 and b4-b6), because water stored above the membrane gradually leaks through the left and right edges of the membrane following soil matric potential gradients. However, the water leaking rate for the deformed soil is smaller than the rate for the non-deformed soil, such that in Fig. 11b4-b6, relatively large soil water contents can be observed compared to Fig. 11a4-a6. That is because surface compaction could decrease the soil hydraulic conductivity near the edges of the subsurface membrane, marked with two arrows in Fig. 11b4. Hence, the liquid water above the membrane is partially trapped above the subsurface membrane.

When presenting Fig. 11, we use a relatively large color contrast in the high water content regions (mainly above the subsurface membrane). Therefore, the color changes between cyan and dark blue in

Fig. 11b5 and b6 imply a relatively small water content fluctuation. Moreover, when surface infiltration is terminated, we assume the surface is impermeable to liquid water and water vapor fluxes, such that the water cumulated above the membrane in Fig. 11b4–b6 can be obvious. In reality, the surface water could be lost via evaporation, and therefore, SWRT with "bowl-shape" membranes are supposed to only create high soil water content regions temporarily.

In this example, SWRT can preserve soil water, and its water preserving function relates to the subsurface membrane geometry and soil deformation. However, water stored by the membrane should be used before it leaks away. In general, the geometric configuration of the "bowl-shape" membranes, the depth of burial, the irrigation method (surface or subsurface) and the soil properties may vary in field experiments (For example, in Guber et al., 2015, coarse sand is used, and the bowl-shape membranes are placed at multiple places). Thus, this example mainly illustrates a potential application of the proposed model framework. Moreover, potential applications of the model framework are not limited to SWRT but can be expanded to a variety of soil and agriculture problems, such as (interrow) subsurface irrigation under surface compaction or surface covering.

6. Conclusion

In this study, a model framework of the coupled heat and water transfer (CHWT) problem is presented. First, a baseline mixed FEM scheme is formulated for the fully coupled CHWT governing equations. Soil water potential, temperature, liquid water flux, vapor flux and conductive heat flux are explicitly solved, and local and global conservation of mass and energy are achieved. Second, an adaptive mesh refinement is designed to improve the simulation accuracy and resolution under spatial variations of soil properties. Gradient measure and clustering model trace the spatial variations, and nested FEM mesh grid and "virtual-split" process facilitate the mesh refinement for the mixed FEM solver. Third, a mesh deformation model for soil non-rigidity is presented. When external load exists, soil deformation is computed using an updated Lagrangian formulation, and the deformation results are transferred to the CHWT model via the deformed mesh grid. Therefore, the model framework proposed in this study provides a generic and adaptive way to perform CHWT simulations in non-rigid soils with spatial variations of soil properties.

The main accomplishment of this study is the model establishment. The illustrative examples are typical soil physics problems or abstracted from real-world applications. In addition, using the "k-means" model is an attempt to include machine learning methods in soil process-based models. The soil hydraulic and thermal properties, as well as the empirical stress–strain relations can be updated to improve real-world applications without substantial changes of the model architecture. Obtaining systematic constitutive relations for soil strain–stress and soil hydraulic and thermal properties under soil deformation is critical but challenging. Therefore, it should be treated as a future research topic.

Future studies should also include the following topics. (a) In nearly saturated soil, soil compaction may cause water exfiltration and surface runoff, and low temperature may freeze the water in surface soil. Therefore, the CHWT model should be combined with soil surface models or freezing-thawing models (Wang et al., 2020; Wang et al., 2021a, Zheng et al., 2021). (b) The three transfer components, including the liquid water, vapor and conductive heat fluxes in Eq. (1), can be expressed in a partially coupled form (Wang et al., 2022; Luo et al., 2022), and the mixed FEM scheme can be revised for each component to facilitate a modularized programming architecture similar to the existing HYDRUS or 2DSOIL simulators (Saito et al., 2006; Timlin et al., 1996). (c) The numerical scheme can be generalized to include crop growth, root development and soil-root interaction models (Wang et al., 2021b). (d) With a tetrahedral mesh grid, the model framework can be generalized to 3D soil CHWT simulations.

Data availiability

The model proposed in this study will be available at (https://github.com/cauwzj). Model development and validation examples are composed in a supplementary material and released in that repository. Soil data in the validation examples can be found in Celia et al. (1990) and Heitman et al. (2008).

CRediT authorship contribution statement

Zhuangji Wang: Conceptualization, Data curation, Formal analysis, Investigation, Methodology, Software, Validation, Visualization, Writing – original draft. Dennis Timlin: Conceptualization, Data curation, Formal analysis, Investigation, Methodology, Project administration, Resources, Software, Supervision, Validation, Visualization, Writing - review & editing. Gang Liu: Conceptualization, Formal analysis, Methodology, Writing - review & editing. David Fleisher: Conceptualization, Formal analysis, Investigation, Methodology, Validation, Writing - review & editing. Wenguang Sun: Formal analysis, Investigation, Methodology, Visualization, Writing - review & editing. Sahila Beegum: Conceptualization, Formal analysis, Investigation, Methodology, Validation, Writing – review & editing. Joshua Heitman: Conceptualization, Formal analysis, Investigation, Methodology, Resources, Software, Supervision, Validation, Writing – review & editing. Tusheng Ren: Conceptualization, Formal analysis, Investigation, Methodology, Software, Supervision, Validation, Writing - review & editing. Yan Chen: Conceptualization, Formal analysis, Investigation, Methodology, Software, Supervision, Validation, Writing - review & editing. Vangimalla R. Reddy: Funding acquisition, Project administration, Resources, Supervision, Writing – review & editing. Katherine Tully: Funding acquisition, Investigation, Methodology, Project administration, Resources, Supervision, Writing - review & editing. Robert Horton: Conceptualization, Formal analysis, Funding acquisition, Investigation, Methodology, Supervision, Writing - review & editing.

Declaration of competing interest

The authors declare that they have no known competing financial interests or personal relationships that could have appeared to influence the work reported in this paper.

Acknowledgements

This material is based upon work supported by the Department of Agriculture, Agricultural Research Service under Agreement No. 58-8042-7-067, National Science Foundation under Grant 2037504, and USDA-NIFA Multi-State Project 4188. The authors also received support from the University of Maryland at College Park, University of Nebraska at Lincoln, China Agricultural University, North Carolina State University, and Iowa State University.

References

- Aarnes, J.E., Efendiev, Y., Jiang, L., 2008. Mixed multiscale finite element method using limited global information. SIAM Multiscale Model. Simul. 7, 655–676. https://doi. org/10.1137/070688481.
- Ankeny, M.D., Kaspar, T.C., Horton, R., 1988. Design for an automated tension infiltrometer. Soil Sci. Soc. Am. J. 52, 893–896. https://doi.org/10.2136/ sssai1988.03615995005200030054x.
- Bathe, K.-J., 2014. Finite element procedures, 2nd Edition. Prentice-Hall, Pearson Education Inc.
- Boffi, D., Brezzi, F., Fortin, M., 2013. Mixed finite element methods and applications. Springer Series in Computational Mathematics 44. https://doi.org/10.1007/978-3-642-36519-5.
- Brezzi, F., 1974. On the existence, uniqueness and approximation of saddle point problems arising from lagrangian multipliers. r.a.i.r.o. Analyse Numérique. 8, 129–151. https://doi.org/10.1051/m2an/197408R201291.

- Canny, J., 1986. A computational approach to edge detection. IEEE trans. Pattern Analysis and Machine Intelligence. 8, 679–698. https://doi.org/10.1109/ TPAMJ 1986 4767851
- Cass, A., Campbell, G.S., Jones, T.L., 1984. Enhancement of thermal water vapor diffusion in soil. Soil Sci. Soc. Am. J. 48, 25–32. https://doi.org/10.2136/ sssaj1984.03615995004800010005x.
- Celia, M.A., Bouloutas, E.T., Zabra, R.L., 1990. A general mass-conservative numerical solution for the unsaturated flow equation. Water Resour. Res. 26, 1483–1496. https://doi.org/10.1029/WR026i007p01483.
- Chen, Y., Durlofsky, L.J., Gerritsen, M., Wen, X.H., 2003. A coupled local–global upscaling approach for simulating flow in highly heterogeneous formations. Adv. Water Resour. 26, 1041–1060. https://doi.org/10.1016/S0309-1708(03)00101-5.
- Chounet, L.M., Hilhorst, D., Jouron, C., Kelanemer, Y., Nicolas, P., 1999. Simulation of water flow and heat transfer in soils by means of a mixed finite element method. Adv. Water Resour. 22, 445–460. https://doi.org/10.1016/S0309-1708(98)00029-3
- Clément, J.-B., Golay, F., Ersoy, M., Sous, M., 2021. An adaptive strategy for discontinuous galerkin simulations of Richards' equation: application to multimaterials dam wetting. Adv. Water. Resour. 151, 103897.
- Côté, J., Konrad, J.-M., 2005. A generalized thermal conductivity model for soils and construction materials. Canadian Geotechnical Journal. 42, 443–458. https://doi. org/10.1139/t04-106.
- Durlofsky, L.J., Efendiev, Y., Ginting, V., 2007. An adaptive local–global multiscale finite volume element method for two-phase flow simulations. Adv. Water Resour. 30, 576–588. https://doi.org/10.1016/j.advwatres.2006.04.002.
- Efendiev, Y., Hou, T.Y., 2009. Multiscale Finite Element Methods, Surveys and Tutorials in the Applied Mathematical Sciences, vol. 4. Springer, New York.
- Fredlund, D.G., Rahardjo, H., Fredlund, M.D., 2012. Unsaturated soil mechanics in engineering Practice. John Wiley & Sons, Inc, 10.1002/9781118280492.
- Géron, A., 2019. Hands-on machine learning with scikit-learn, keras, and tensorflow, (2nd ed.). O'Reilly Media Inc.
- Guber, A.K., Smucker, A.J.M., Berhanu, S., Miller, J.M.L., 2015. Subsurface water retention technology improves root zone water storage for corn production on coarse-textured soils. Vadose Zone J. 14 https://doi.org/10.2136/vzj2014.11.0166.
- He, X., Ren, L., 2005. Finite volume multiscale finite element method for solving the groundwater flow problems in heterogeneous porous media. Water Resour. Res. 41, W10417. https://doi.org/10.1029/2004WR003934.
- He, X., Ren, L., 2006. A multiscale finite element linearization scheme for the unsaturated flow problems in heterogeneous porous media. Water Resour. Res. 42, W08417. https://doi.org/10.1029/2006WR004905.
- He, X., Ren, L., 2009. An adaptive multiscale finite element method for unsaturated flow problems in heterogeneous porous media. J. Hydrol. 374, 56–70. https://doi.org/ 10.1016/j.jhydrol.2009.05.021.
- Heitman, J.L., Horton, R., Ren, T., Ochsner, T.E., 2007. An improved approach for measurement of coupled heat and water transfer in soil cells. Soil Sci. Soc. Am. J. 71, 872–880. https://doi.org/10.2136/sssaj2006.0327.
- Heitman, J.L., Horton, R., Ren, T., Nassar, I.N., Davis, D.D., 2008. A test of coupled soil heat and water transfer prediction under transient boundary temperatures. Soil Sci. Soc. Am. J. 72. 1197–1207. https://doi.org/10.2136/sssaj2007.0234.
- Hou, T.Y., Wu, X., 1997. A multiscale finite element method for elliptic problems in composite materials and porous media. J. Comput. Phys. 134, 169–189. https://doi. org/10.1006/jcph.1997.5682.
- Hou, T.Y., Wu, X., Cai, Z., 1999. Convergence of multi-scale finite element method for elliptic problems with rapidly oscillating coefficients. Math. Comput. 68, 913–943. https://doi.org/10.1090/S0025-5718-99-01077-7.
- Hunter, J.K., 2004. Asymptotic analysis and singular perturbation theory. University of California at Davis, Department of Mathematics.
- Jiang, L., Efendiev, Y., Mishev, I., 2010. Mixed multiscale finite element methods using approximate global information based on partial upscaling. Comput. Geosci. 14, 319–341. https://doi.org/10.1007/s10596-009-9165-7.
- Lewis, R.W., Schrefler, B.A., 1999. The finite element method in the static and dynamic deformation and consolidation of porous media, 2nd Edition. John Wiley & Sons
- Li, S., Wang, C., Shi, L., Yin, N., 2019. Statistical characteristics of the thermal conductivity of frozen clay at different water contents. Results Phys. 13, 102179 https://doi.org/10.1016/j.rinp.2019.102179.
- Li, N., Yue, X., Ren, L., 2016. Numerical homogenization of the Richards equation for unsaturated water flow through heterogeneous soils. Water Resour. Res. 52, 8500–8525. https://doi.org/10.1002/2015WR018508.
- Lu, Y., Lu, S., Horton, R., Ren, T., 2014. An empirical model for estimating soil thermal conductivity from texture, water content, and bulk density. Soil Sci. Soc. Am. J. 78, 1859–1868. https://doi.org/10.2136/sssaj2014.05.0218.
- Luo, C., Wang, Z., Kordbacheh, F., Zhang, Y., Yang, B., Kim, S., Cetin, B., Ceylan, H., Horton, R., 2019. The influence of concrete grinding residue on soil physical properties and plant growth. J. Environ. Qual. https://doi.org/10.2134/ iea2019.06.0229.
- Luo, C., Shi, Y., Timlin, D., Ewing, R., Fleisher, D., Horton, R., Tully, K., Wang, Z., 2022. A multiscale finite element method for coupled heat and water transfer in heterogeneous soils. J. Hydrol. 612, 128028 https://doi.org/10.1016/j. ibydrol.2022.128028
- McCullough, M.C., Parker, D.B., Robinson, C.A., Auvermann, B.W., 2001. Hydraulic conductivity, bulk density, moisture content, and electrical conductivity of a new sandy loam feedlot surface. ASABE. Appl. Eng. Agric. 17 (539–544) https://doi.org/ 10.13031/2013.6471.
- Milly, P.C.D., 1982. Moisture and heat transport in hysteretic, inhomogeneous porous media: a matric head-based formulation and a numerical model, water resour. Res. 18, 489–498. https://doi.org/10.1029/WR018i003p00489.

- Mohanty, B.P., Ankeny, M.D., Horton, R., Kanwar, R.S., 1994. Spatial analysis of hydraulic conductivity measured using disc infiltrometers. Water Resour. Res. 30, 2489–2498. https://doi.org/10.1029/94WR01052.
- Nassar, I.N., Horton, R., 1989. Water transport in unsaturated nonisothermal salty soil: II. theoretical development. Soil Sci. Soc. Am. J. 53, 1330–1337. https://doi.org/ 10.2136/sssaj1989.03615995005300050005x.
- Nassar, I.N., Horton, R., 1997. Heat, water, and solution transfer in unsaturated porous media: I theory development and transport coefficient evaluation. Transport Porous Med. 27, 17–38. https://doi.org/10.1023/A:1006583918576.
- Nishiwaki, J., Horton, R., 2020. Temporal changes in soil hydraulic conductivity in saturated and unsaturated fields. Paddy Water Environ. 18, 677–686. https://doi org/10.1007/s10333-020-00810-x.
- Pan, L., Warrick, A.W., Wierenga, P.J., 1996. Finite element methods for modeling water flow in variably saturated porous media: numerical oscillation and mass-distributed schemes. Water Resour. Res. 32, 1883–1889. https://doi.org/10.1029/96WR00753.
- Peng, C., Wu, W., Yu, H., Wang, C., 2015. A SPH approach for large deformation analysis with hypoplastic constitutive model. Acta Geotech. 10, 703–717. https://doi.org/ 10.1007/s11440-015-0399-3.
- Philip, R., de Vries, D.A., 1957. Moisture movement in porous materials under temperature gradients. Trans. Am. Geophys. Union. 38, 222–232. https://doi.org/ 10.1029/TB038i002a00222
- Phoon, K.K., Huang, S.P., Quek, S.T., 2002. Simulation of second-order processes using Karhunen-loeve expansion. Comput. Struct. 80, 1049–1060. https://doi.org/10.1016/S0045-7949(02)00064-0.
- Phoon, K.K., Huang, H.W., Quek, S.T., 2005. Simulation of strongly non-gaussian processes using Karhunen-loeve expansion. Probabilistic Eng. Mech. 20, 188–198. https://doi.org/10.1016/j.probengmech.2005.05.007.
- Putti, M., Sartoretto, F., 2009. Linear galerkin vs mixed finite element 2D flow fields. Int. J. Numer. Meth. Fluids 60, 1011–1031. https://doi.org/10.1002/fld.1929.
- Rienzner, M., Gandolfi, C., 2014. Investigation of spatial and temporal variability of saturated soil hydraulic conductivity at the field-scale. Soil Tillage Res. 135, 28–40. https://doi.org/10.1016/j.still.2013.08.012.
- Saito, H., Simunek, J., Mohanty, B.P., 2006. Numerical analysis of coupled water, vapor, and heat transport in the vadose zone. Vadose Zone J. 5, 784–800. https://doi.org/10.2136/vzi2006.0007.
- Shangguan, W., Dai, Y., Duan, Q., Liu, B., Yuan, H., 2014. A global soil data set for earth system modelling. J. Adv. Model. Earth Syst. 6, 249–263. https://doi.org/10.1002/ 2013MS000293.
- Simunek, J., van Genuchten, M.T., Sejna, M., 2016. Recent developments and applications of the hydrus computer software packages. Vadose Zone J. 15, 1–25. https://doi.org/10.2136/vzi2016.04.0033.
- Sophocleous, M., 1979. Analysis of water and heat flow in unsaturated-saturated porous media. Water Resour. Res. 15, 1195–1206. https://doi.org/10.1029/ WR015i005p01195.
- Tian, Z., Kool, D., Ren, T., Horton, R., Heitman, J., 2019. Approaches for estimating unsaturated soil hydraulic conductivities at various bulk densities with the extended mualem-van genuchten model. J. Hydrol. 572, 719–731. https://doi.org/10.1016/j. ibydrol.2019.03.027
- Tian, Z., Chen, J., Cai, C., Gao, W., Ren, T., Heitman, J., Horton, R., 2021. New pedotransfer functions for soil water retention curves that better account for bulk density effects. Soil Tillage Res. 205, 104812 https://doi.org/10.1016/j. still.2020.104812.
- Timlin, D., Pachepsky, Y.A., Acock, B., 1996. A design for a modular, generic soil simulator to interface with plant models. Agron. J. 88, 162–169. https://doi.org/ 10.2134/agronj1996.00021962008800020008x.

- Vanderborght, J., Fetzer, T., Mosthaf, K., Smits, K.M., Helmig, R., 2017. Heat and water transport in soils and across the soil-atmosphere interface: 1. theory and different model concepts. Water Resour. Res. 53, 1057–1079. https://doi.org/10.1002/ 2016WR019982
- Wang, Z., Ankeny, M., Horton, R., 2017. The impact of water vapor diodes on soil water redistribution. J. Hydrol. 552, 600–608. https://doi.org/10.1016/j. ibydrol.2017.07.009
- Wang, Z., Timlin, D., Kouznetsov, M., Fleisher, D., Li, S., Tully, K., Reddy, V.R., 2020.
 Coupled model of surface runoff and surface-subsurface water movement. Adv.
 Water Resour. 137, 103499 https://doi.org/10.1016/j.advwatres.2019.103499.
- Wang, Z., Thapa, R., Timlin, D., Li, S., Sun, W., Beegum, S., Fleisher, D., Mirsky, S., Cabrera, M., Sauer, T., Reddy, V.R., Horton, R., Tully, K., 2021a. Simulations of water and thermal dynamics for soil surfaces with residue mulch and surface runoff. Water Resour. Res. 57 https://doi.org/10.1029/2021WR030431.
- Wang, Z., Timlin, D., Li, S., Fleisher, D., Dathe, A., Luo, C., Dong, L., Reddy, V.R., Tully, K., 2021b. A diffusive model of maize root growth in MAIZSIM and its applications in ridge-furrow rainfall Harvesting. Agri. Water Manag. 254, 106966 https://doi.org/10.1016/j.agwat.2021.106966.
- Wang, Z., Timlin, D., Fleisher, D., Sun, W., Beegum, S., Li, S., Chen, Y., Reddy, V.R., Tully, K., and Horton, R., 2022. Modeling vapor transfer in soil water and heat simulations: a modularized, partially-coupled approach. J. Hydrol. 608, 127541 https://doi.org/10.1016/j.jhydrol.2022.127541.
- Wang, X.T., Wu, W., 2009. An update hypoplastic constitutive model, its implementation and application in tunnelling. University of Natural Resources and Applied Life Sciences, Vienna https://epub.boku.ac.at/obvbokhs/content/titleinfo/1931763/ full.pdf.
- Wang, X.T., Wu, W., 2011. An update hypoplastic constitutive model, its implementation and application. In: Wan, R., Alsaleh, A., Nghiem, L. (Eds.), Bifurcations, Instabilities and Degradations in Geomaterials. Springer, Berlin, pp. 133–143.
- Winkler, G., 2003. Image analysis, random fields and Markov chain Monte Carlo methods: a mathematical introduction. Springer Science & Business Media.
- Xie, K.H., Leo, C.J., 2004. Analytical solutions of one-dimensional large strain consolidation of saturated and homogeneous clays. Comput. Geotech. 31, 301–314. https://doi.org/10.1016/j.compgeo.2004.02.006.
- Xie, X., Lu, Y., Ren, T., Horton, R., 2018. An empirical model for estimating soil thermal diffusivity from texture, bulk density, and degree of saturation. J. Hydrometeorol. 19, 445–457. https://doi.org/10.1175/JHM-D-17-0131.1.
- Yuan, W.H., Zhang, W., Bai, B., Wang, Y., 2019. Application of the particle finite element method for large deformation consolidation analysis. Eng. Comput. 36, 3138–3163. https://doi.org/10.1108/EC-09-2018-0407.
- Zhang, M., Tian, Ž., Zhu, Q., Chen, J., 2023. In-situ assessment of soil shrinkage and swelling behavior and hydro-thermal regimes with a thermo-time domain reflectometry technique. Soil Tillage Res. 227, 105617 https://doi.org/10.1016/j. still.2022.105617
- Zhang, W., Zhong, Z.H., Peng, C., Yuan, W.H., Wu, W., 2021. GPU-accelerated smoothed particle finite element method for large deformation analysis in geomechanics. Comput. Geotech. 129, 103856 https://doi.org/10.1016/j.compgeo.2020.103856.
- Zheng, C., Simunek, J., Zhao, Y., Lu, Y., Liu, X., Shi, C., Li, H., Yu, L., Zeng, Y., Su, Z., 2021. Development of the hydrus-1D freezing module and its application in simulating the coupled movement of water, vapor, and heat. J. Hydrol. 598, 126250 https://doi.org/10.1016/j.jhydrol.2021.126250.